

Alexander Edström

# Theoretical Magnet Design

*From the electronic structure of solid matter to new  
permanent magnets.*



UPPSALA  
UNIVERSITET

## Abstract

A good permanent magnet should possess a large saturation magnetisation ( $M_s$ ), large magnetocrystalline anisotropy energy (MAE) and a high Curie temperature ( $T_C$ ). A difficult but important challenge to overcome for a sustainable permanent magnet industry is to find novel magnetic materials, exhibiting a large MAE, without the use of scarcely available elements such as rare-earth metals. The purpose of this thesis is to apply computational methods, including density functional theory and Monte Carlo simulations, to assess the three above mentioned permanent magnet properties and in particular to discover new replacement materials with large MAE without the use of critical materials such as rare-earths.

One of the key results is the theoretical prediction of a tetragonal phase of  $\text{Fe}_{1-x}\text{Co}_x\text{-C}$  with large  $M_s$  and significantly increased MAE which is later also experimentally confirmed. Furthermore, other potential materials are surveyed and in particular the properties of a number of binary alloys in the  $\text{L1}_0$  structure,  $\text{FeNi}$ ,  $\text{CoNi}$ ,  $\text{MnAl}$  and  $\text{MnGa}$ , are thoroughly investigated and shown to possess the desired properties under certain conditions.

## Acknowledgements

Firstly, I wish to thank my supervisor, Jan Ruzs, for all his kind and invaluable guidance through the work behind this thesis. I also thank my second supervisor, Olle Eriksson, for sharing his knowledge and wisdom as well as for providing a positive and encouraging research environment at the division of materials theory. Furthermore, I would like to thank Mirosław Werwiński and Pablo Maldonado for their company, for answering many questions, questioning many answers and for all the discussions on physics, Feynman, Bonobos and all the other stuff. Finally, I am grateful to all my other colleagues at the division of materials theory, those I have worked with at other parts of the Ångström laboratory and to collaborators from the REFREPERMAG project.



# List of papers

This thesis is based on the following papers, which are referred to in the text by their Roman numerals.

- I Stabilization of the tetragonal distortion of  $\text{Fe}_x\text{Co}_{1-x}$  alloys by C impurities - a potential new permanent magnet**  
E. K. Delczeg-Czirjak, A. Edström, M. Werwiński, J. Ruzs, N. V. Skorodumova, L. Vitos, and O. Eriksson.  
Phys. Rev. B **89**, 144403 (2014).
- II Increased magnetocrystalline anisotropy in epitaxial Fe-Co-C thin films with spontaneous strain**  
L. Reichel, G. Giannopoulos, S. Kauffman-Weiss, M. Hoffmann, D. Pohl, A. Edström, S. Oswald, D. Niarchos, J. Ruzs, L. Schultz, S. Fähler.  
*Submitted.*
- III Electronic structure and magnetic properties of  $\text{L1}_0$  binary alloys**  
A. Edström, J. Chico, A. Jakobsson, A. Bergman, J. Ruzs.  
Phys. Rev. B **90**, 014402 (2014) .

Reprints were made with permission from the publishers.



# Contents

1	Introduction .....	9
2	Elements of the Theory of Magnetism .....	11
2.1	Relativistic Electrons .....	11
2.1.1	Non-Relativistic Limit and the Scalar Relativistic Approximation .....	13
2.1.2	Spin-Orbit Coupling and the Magnetocrystalline Anisotropy .....	14
2.2	Exchange Interactions and the Heisenberg Hamiltonian .....	16
3	Computational Methods .....	21
3.1	Density Functional Theory .....	21
3.1.1	FP-LAPW .....	23
3.1.2	SPR-KKR .....	23
3.1.3	Models to Treat Disorder .....	24
3.1.4	Computing the MAE .....	26
3.1.5	Exchange Coupling Parameters .....	30
3.2	Monte Carlo Simulations .....	30
4	Results .....	33
4.1	$\text{Fe}_{1-x}\text{Co}_x$ Alloys .....	33
4.1.1	$(\text{Fe}_{1-x}\text{Co}_x)\text{-C}$ .....	34
4.1.2	$(\text{Fe}_{1-x}\text{Co}_x)\text{-B}$ .....	35
4.2	$\text{L1}_0$ Binary Compounds .....	36
4.3	Other Potential Materials .....	38
4.3.1	$(\text{Fe}_{1-x}\text{Co}_x)_2\text{B}$ .....	38
4.3.2	Heusler Alloys .....	40
5	Conclusions .....	42
	References .....	44





# 1. Introduction

Albeit being a phenomena known since ancient times, to this day magnetism remains under vast research activity due to its theoretical complexity and far-reaching technological importance. One important field for magnetic materials is found in the area of permanent magnets [1, 2, 3, 4, 5] with applications in large scale industries including those for motors, generators and actuators. With a growing demand from emerging industries, such as that of wind power generation, the need of sustainable high performance permanent magnets is greater than ever.

In the last decades of the 20th century came the development of permanent magnets consisting of compounds of rare-earths and transition metals, such as  $\text{SmCo}_5$  and  $\text{Nd}_2\text{Fe}_{14}\text{B}$  which to this day possess properties superior to all alternatives. However, in recent years due to economic reasons, a need for alternative materials which do not contain rare-earth elements has arisen [6, 1, 4]. The figures of merit of a permanent magnet are the coercivity  $H_c$  and the energy product  $(BH)_{\max}$ , and in addition to this a high Curie temperature is needed in order for the magnets to operate with good performance at reasonable temperatures. The extrinsic property requirement of high coercivity and large energy product translates, in terms of intrinsic properties, into a large saturation magnetisation  $M_s$  and magnetocrystalline anisotropy energy (MAE). Table 1.1 contains a summary of relevant properties of some of the most common rare-earth permanent magnets, one of the common alternative materials, namely ferrite magnet  $\text{BaFe}_{12}\text{O}_{19}$  and for comparison also transition metals bcc Fe and hcp Co. It is apparent that the remarkable properties of the rare-earth based magnets stem from their large MAE. As a matter, of fact the cheap and highly abundant bcc Fe has higher  $M_s$  and  $T_C$  than the rare-earth magnets, but the MAE is orders of magnitude smaller making bcc Fe useless as a permanent magnet. As will become clear in chapter 2 there are two reasons for the MAE being so low in Fe while it is so high in for example  $\text{Nd}_2\text{Fe}_{14}\text{B}$ ; first of all the cubic bcc crystal of Fe does not allow for the large MAE mainly found in uniaxial crystals and secondly the MAE is closely related to the spin-orbit coupling which tends to be strong in heavy elements in the lower part of the periodic table. These elements are often also less abundant which is the main challenge in finding new materials suitable as permanent magnets and the main purpose of this thesis is to provide potential solutions to this problem.

One useful path to finding new materials with the desired properties is through computational methods, such as electronic structure calculations, which

**Table 1.1.** A summary of the properties of some high performing rare-earth magnets, a ferrite alternative and the transition metals bcc Fe and hcp Co. The relevant permanent magnet properties provided are Curie temperature ( $T_C$ ), coercivity ( $H_c$ ), energy product ( $(BH)_{\max}$ ), saturation magnetisation ( $M_s$ ), and magnetocrystalline anisotropy energy (MAE). Data was taken from Ref. [1, 7, 8]. The extrinsic properties depend on the microstructure of the material and should be considered an estimate of what is practically realisable.

	Nd <sub>2</sub> Fe <sub>14</sub> B	SmCo <sub>5</sub>	BaFe <sub>12</sub> O <sub>19</sub>	bcc Fe	hcp Co
$T_C$ (K)	588	1020	740	1043	1388
$\mu_0 H_c$ (T)	1.21	0.90	0.15	$7 \cdot 10^{-5}$	$5 \cdot 10^{-3}$
$(BH)_{\max}$ (kJ/m <sup>3</sup> )	512	231	45	-	-
$\mu_0 M_s$ (T)	1.61	1.22	0.48	2.21	1.81
MAE (MJ/m <sup>3</sup> )	4.9	17.2	0.33	0.048	0.53

allow for exploring the properties of various materials with relative ease compared to experimental work and it is this path which is to be taken in this thesis. Density functional theory (DFT) provides a powerful tool for studying the electronic structure and ground state properties of materials, including the  $M_s$  and MAE which are essential for permanent magnets. In combination with other computational methods, such as Monte Carlo (MC) simulations, also the Curie temperature can be determined and hence all of the three main properties of interest are obtainable.

This thesis will begin with an overview of those parts of the theory of magnetism especially important for this work in Chapter 2. In particular the relativistic spin-orbit coupling and its relation to MAE will be brought up in Sec. 2.1 and exchange interactions and the Heisenberg Hamiltonian which result in spontaneous magnetic ordering will be briefly discussed in Sec. 2.2. The relevant computational methods will then be introduced in Chapter 3 with DFT being discussed in Sec. 3.1 and MC in 3.2. In Chapter 4 the main results, based on the work presented in papers I-III, are summarized. These results mainly regard two groups of materials. Firstly C-doping is suggested as a method of causing a tetragonal distortion in FeCo alloys in paper I, which is then experimentally realized in paper II. The properties of various binary alloys in the L1<sub>0</sub> structure are then explored in paper III and found to show promising qualities under certain conditions. In addition to this a brief survey is given over other materials which might be of interest in a permanent magnet context.

## 2. Elements of the Theory of Magnetism

This chapter gives an introduction and overview of those areas of the theory of magnetism which are most important to understand the theoretical aspects of permanent magnets most relevant to the work behind this thesis. It begins, in Sec. 2.1, by discussing the relativistic nature of magnetism and in particular in Sec. 2.1.2, the spin-orbit coupling and its relation to the magnetocrystalline anisotropy. It continues in Sec. 2.2 by discussing the exchange interactions which lead to magnetic ordering and how it can be described in terms of exchange coupling parameters and the Heisenberg Hamiltonian.

### 2.1 Relativistic Electrons

Magnetism arises due to the quantum mechanical spin or orbital angular momentum of electrons. The spin angular momentum was initially rather artificially introduced into the theory of quantum mechanics to explain the fine structure of the hydrogen atom [9]. It was not until Dirac introduced a relativistic wave equation [10, 11] for the electron that the spin became well understood as an intrinsic angular momentum necessary for a Lorentz symmetric version of quantum mechanics. Moreover, relativistic effects neglected in the Schrödinger equation are of importance in describing electrons in atomic core states and the relativistic spin-orbit coupling, which will be discussed further later on, brings in a rich new array of physical phenomena including the magnetocrystalline anisotropy which is essential for the field of permanent magnets.

The Dirac equation may, including electromagnetic interactions, be written in the following way [12]

$$\left[ \gamma^\mu (i\partial_\mu - eA_\mu) - m \right] \psi = 0, \quad (2.1)$$

where  $e$  is the electron charge,  $\gamma^\mu$  are the Dirac matrices,  $A_\mu$  is the electromagnetic potential and  $m$  is the electron mass. Alternatively it might, after separating out the time dependence, be written

$$[\alpha \cdot (-i\nabla - e\mathbf{A}) + eV + \beta m] \psi = E\psi, \quad (2.2)$$

where  $\mathbf{A}$  is the magnetic vector potential,  $V$  is the scalar potential,

$$\beta = \gamma^0 = \begin{pmatrix} \mathbb{I}_{2 \times 2} & 0 \\ 0 & -\mathbb{I}_{2 \times 2} \end{pmatrix} \quad \text{and} \quad \alpha = \begin{pmatrix} 0 & \boldsymbol{\sigma} \\ \boldsymbol{\sigma} & 0 \end{pmatrix}, \quad (2.3)$$

where  $\sigma = (\sigma_x, \sigma_y, \sigma_z)$  contains the Pauli matrices. In principle, Eq. 2.2 will provide all of the information required to understand the magnetic phenomena discussed here and it is the equation which is solved for all electrons in the SPR-KKR method and for the core electrons only in the FP-LAPW method, as will be further discussed in Sections 3.1.1-3.1.2. Often however, solving Eq. 2.2 is more complicated than what is necessary to describe the phenomena of interest with good accuracy, so that simplifications and approximations can beneficially be applied. One such simplification is to expand the equation in the non-relativistic limit  $v/c \ll 1$  as discussed in Sec. 2.1.2. This naturally introduces a term describing the spin-orbit coupling, which is essential for magnetocrystalline anisotropy, and allows for applying the so called scalar relativistic approximation.

For spherically symmetric potentials, such as the Coulomb potential for hydrogen-like atoms, certain exact analytical results can be obtained for the Dirac equation [12, 13]. The solution may in general be written [12]

$$\psi_{j,m}^k(r, \theta, \phi) = \begin{pmatrix} f^k(r) \mathcal{Y}_{j,m}^k(\theta, \phi) \\ ig^k(r) \mathcal{Y}_{j,m}^{-k}(\theta, \phi) \end{pmatrix}, \quad (2.4)$$

where  $f$  and  $g$  are two-component radial dependent functions,  $\mathcal{Y}_{j,m}^k(\theta, \phi)$  are generalised spherical harmonics,  $j, m$  denote the total angular momentum quantum numbers and

$$k = \begin{cases} l & \text{if } l = j + \frac{1}{2} \\ -(l+1) & \text{if } l = j - \frac{1}{2} \end{cases} \quad (2.5)$$

is a quantum number related to the parity of the solution. The generalised spherical harmonics are related to regular spherical harmonics,  $Y_{l,m}$ , according to

$$\mathcal{Y}_{j,m}^k(\theta, \phi) = -\text{sgn} k \sqrt{\frac{k + \frac{1}{2} - m}{2k+1}} \alpha Y_{l,m-\frac{1}{2}} + \sqrt{\frac{k + \frac{1}{2} + m}{2k+1}} \beta Y_{l,m+\frac{1}{2}}, \quad (2.6)$$

where

$$\alpha = \begin{pmatrix} 1 \\ 0 \end{pmatrix} \quad \beta = \begin{pmatrix} 0 \\ 1 \end{pmatrix}. \quad (2.7)$$

Here can be noted that the orbital or spin angular momentum operators individually do not commute with the Dirac Hamiltonian while total angular momentum and parity do. Typically in solid matter, those electrons for which relativistic effects tend to be important are tightly bound core states. These are also, to a very good approximation, in a spherical potential so that it is appropriate to describe them with solutions of the form given in Eq. 2.4.

### 2.1.1 Non-Relativistic Limit and the Scalar Relativistic Approximation

If one does not wish to work with the full four-component Dirac formalism introduced in the previous section but still wishes to retain certain relativistic effects, it is appropriate to make an expansion in the non-relativistic limit,  $\frac{v}{c} \ll 1$ , and only keep terms up to a certain order. The first step in doing so is to assume a solution of the form [12]

$$\psi(\mathbf{r}) = \begin{pmatrix} \chi(\mathbf{r}) \\ \eta(\mathbf{r}) \end{pmatrix}, \quad (2.8)$$

where  $\chi$  and  $\eta$  each has two components. A useful next step is to perform a Foldy-Wouthuysen transformation, where one introduces a hermitian and unitary operator

$$U = U^{-1} = U^\dagger = A\beta + \frac{\boldsymbol{\alpha} \cdot \mathbf{p}}{2m} \quad A = \sqrt{1 - \frac{p^2}{4m^2}}. \quad (2.9)$$

Transforming the Dirac equation according to  $H' = UHU^{-1}$  and  $\psi' = U\psi$ , performing some algebra and eventually only keeping terms to order  $\left(\frac{v}{c}\right)^2$  leads to a decoupling of  $\chi$  and  $\eta$  and a Hamiltonian

$$H = \frac{(\mathbf{p} - e\mathbf{A})^2}{2m} + eV - \frac{e}{2m} \boldsymbol{\sigma} \cdot \mathbf{B} - \frac{p^4}{8c^2m^3} + \frac{e\nabla^2 V}{8c^2m^2} + \frac{e\hbar}{4c^2m^2} \boldsymbol{\sigma} \cdot (\nabla V \times \mathbf{p}). \quad (2.10)$$

The first three terms in this equation make up the non-relativistic Schrödinger Hamiltonian, including the Zeeman term

$$H_{\text{Zeeman}} = -\frac{e}{2m} \boldsymbol{\sigma} \cdot \mathbf{B}, \quad (2.11)$$

where  $\mathbf{B} = \nabla \times \mathbf{A}$  is the magnetic flux density. After that comes a so called mass correction term  $-\frac{p^4}{8c^2m^3}$ , the Darwin term  $\frac{e\nabla^2 V}{8c^2m^2}$  and finally the spin-orbit coupling (SOC)  $\frac{e}{4c^2m^2} \boldsymbol{\sigma} \cdot (\nabla V \times \mathbf{p})$  which, if one assumes the scalar potential to be spherically symmetric, takes on the more common form

$$H_{\text{SOC}} = \frac{e}{4c^2m^2r} \frac{dV(r)}{dr} \boldsymbol{\sigma} \cdot \mathbf{L} = \xi \mathbf{L} \cdot \mathbf{S}, \quad (2.12)$$

where  $\mathbf{L} = \mathbf{r} \times \mathbf{p}$  is the orbital angular momentum operator,  $\mathbf{S} = \frac{\hbar}{2} \boldsymbol{\sigma}$  is the spin operator and

$$\xi = \frac{e}{2\hbar c^2 m^2 r} \frac{dV(r)}{dr} \quad (2.13)$$

is the spin-orbit coupling constant. Furthermore, for the spherical potential of a hydrogen-like atom, the SOC constant is [7]

$$\xi = \frac{mZ^4 \alpha^4 c^2}{2n^3 l(l + \frac{1}{2})(l + 1)}, \quad (2.14)$$

where  $Z$  is the atomic number,  $\alpha = \frac{e^2}{\hbar c}$  is the fine structure constant and  $n$  and  $l$  denote principal and angular momentum quantum numbers, respectively. From this expression it is clear that the SOC becomes particularly important for states with low angular momentum in heavy atoms with large  $Z$ . This is the source to one of the main challenges in obtaining magnetic materials with large MAE without the use of scarcely available and expensive elements. A large MAE requires a large  $Z$  but materials with  $Z$  significantly larger than the value of  $Z = 26$  for Fe tend to be much less abundant than those elements with smaller  $Z$ . Furthermore, such elements are typically not magnetic.

The above Hamiltonian in Eq. 2.10 acts on a two-component spinor

$$\psi(\mathbf{r}) = \begin{pmatrix} \psi_+ \\ \psi_- \end{pmatrix}, \quad (2.15)$$

where  $\psi_+$  and  $\psi_-$  represent spin up and spin down electrons, respectively. The SOC term is the only term in Eq. 2.10 containing off-diagonal terms and hence coupling the spin up and spin down electrons to each other. Ignoring the SOC and using only the diagonal terms in the Hamiltonian is known as the scalar relativistic approximation.

### 2.1.2 Spin-Orbit Coupling and the Magnetocrystalline Anisotropy

Magnetocrystalline anisotropy is the internal energy dependence on magnetisation direction, i.e.  $E = E(\hat{M})$ , where  $\hat{M} = (\sin \theta \cos \phi, \sin \theta \sin \phi, \cos \theta)$  is the direction of the magnetisation relative to the crystal lattice. This effect was first experimentally observed and described phenomenologically, based on anisotropy constants and crystal symmetries. For example, in a uniaxial crystal the energy may be written [8]

$$E = E_{\text{iso}} + K_1 \sin^2 \theta + K_2 \sin^4 \theta + K_3 \sin^6 \theta + K_4 \sin^6 \theta \cos 6\phi + \dots, \quad (2.16)$$

where  $E_{\text{iso}}$  contains all isotropic energy contributions,  $K_i$  are the anisotropy constants and  $\theta$  and  $\phi$  are the angles describing the magnetisation direction as given above. For a cubic structure on the other hand, the energy is

$$E = E_{\text{iso}} + K_1 (\alpha_1^2 \alpha_2^2 + \alpha_1^2 \alpha_3^2 + \alpha_2^2 \alpha_3^2) + K_2 \alpha_1^2 \alpha_2^2 \alpha_3^2 + \dots, \quad (2.17)$$

where  $\alpha_i$  are the directional cosines of the magnetisation direction.

That the microscopic origin of this anisotropy is related to the SOC, introduced in the previous section, was suggested by Van Vleck [14], as this is the link coupling the spin to the real space crystal symmetry via the orbital angular momentum. If we are mainly interested in the transition metal d-electron magnetism, then the SOC can be considered as a perturbation. The SOC energy

shift to second order is

$$E_{\text{SOC}} = \xi \sum_n \langle n | \mathbf{L} \cdot \mathbf{S} | n \rangle + \xi^2 \sum_{n \neq k} \frac{|\langle n | \mathbf{L} \cdot \mathbf{S} | k \rangle|^2}{E_n - E_k}, \quad (2.18)$$

where  $|n\rangle$  and  $|k\rangle$  denote eigenstates of the unperturbed Hamiltonian and  $E_n$  and  $E_k$  are the associated energy eigenvalues. When considering d-electrons in a solid with a crystal field lifting the degeneracy of the d-orbitals, there is a quenching of orbital angular momentum [15, 16] because  $\langle \mathbf{L} \rangle = \langle i | \mathbf{L} | i \rangle = 0$  for any non-degenerate states  $|i\rangle$ , so that the diagonal matrix elements of the SOC Hamiltonian appearing in the first order term of the perturbation expansion are all zero. Furthermore, if both  $|n\rangle$  and  $|k\rangle$  are occupied or if both are unoccupied, there is a cancellation of terms in the sum so that the only terms which need to be included are those which couple occupied and unoccupied states. Hence, we can express the SOC, based on second order perturbation theory, as

$$E_{\text{SOC}} = \xi^2 \sum_{\substack{\text{occ. } n \\ \text{unocc. } k}} \frac{|\langle n | \mathbf{L} \cdot \mathbf{S} | k \rangle|^2}{E_n - E_k}, \quad (2.19)$$

where the summation is over all occupied states  $|n\rangle$  and unoccupied states  $|k\rangle$ . For uniaxial crystals, the expression in Eq. 2.19 is non-zero and the MAE is of order  $\xi^2$ . For a cubic crystal on the other hand, the second order perturbation term is also zero and one would have to go to fourth order perturbation theory to find non-zero contributions to the MAE [17]. Hence, cubic materials tend to have orders of magnitude smaller MAE than uniaxial ones and this explains why the MAE of bcc Fe is so much smaller than that of hcp Co, as was seen in table 1.1. Therefore, in searching for good permanent magnet materials with large MAE, one should focus on materials with non-cubic crystal structures. Eq. 2.19 also provides another key insight for the search of transition metal based magnets with large MAE. When there is a weak SOC and hence a small  $\xi$ , the only way to obtain a large value for MAE is to have a large number of occupied states  $|n\rangle$  and unoccupied states  $|k\rangle$  with a small energy difference  $E_n - E_k$ . The optimal 3d based permanent magnet material should therefore be one with a uniaxial crystal structure and flat energy bands close to each other just above and below the Fermi energy. This insight was used by Burkert *et al.* [18] to explain the unusually large MAE of certain compositions of tetragonally strained  $\text{Fe}_{1-x}\text{Co}_x$ , which provides an important background for the work in papers I-II, and it is discussed further in Sec. 4.1.1. Similar arguments have also been used, for example, by Costa *et al.* [19] to analyze the large MAE of  $\text{Fe}_2\text{P}$  and insightful illustrations of how the MAE depends sensitively on the band structure around the Fermi energy are provided in Ref. [20].

Based on a perturbation expression such as that in Eq. 2.19, assuming that the exchange splitting is significantly larger than the SOC and ignoring spin-flip terms and deformations of the Fermi surface, Bruno [21] found a simple

relation between the MAE and the orbital moment anisotropy which states that

$$E_{\text{MAE}} = \Delta E_{\text{SOC}} = \frac{\xi}{4} \frac{G}{H} \Delta L = \frac{\bar{\xi}}{4} \Delta L, \quad (2.20)$$

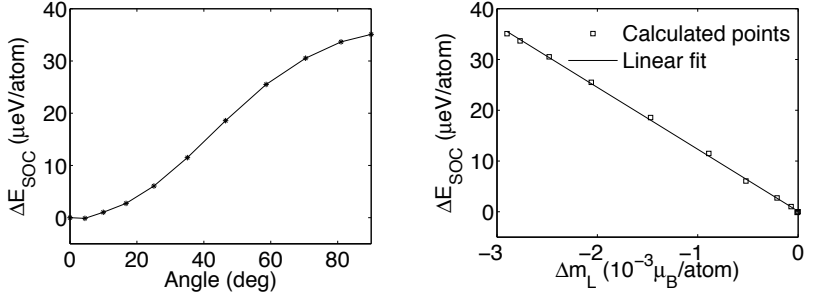
if  $\bar{\xi} = \xi \frac{G}{H}$  and  $G$  and  $H$  are density of states integrals which should often be of similar size so that  $\bar{\xi} \sim \xi$ . Eq. 2.20 tends to give a qualitatively correct description in that there is a proportionality between the change in the orbital moment and the SOC and that the easy axis coincides with the direction where the orbital moment has its maximum. It happens, however, that the relation breaks down, for example due to hybridisation effects in complex materials [22]. On occasion Eq. 2.20 has also been incorrectly applied in explaining the origin of large MAE in transition metal alloys, such as FeNi [23, 24], as being due to anisotropy in the orbital moment. This way of looking at it is incorrect in the sense that Eq. 2.20 does not provide causality in the relation between  $E_{\text{MAE}}$  and  $\Delta L$  but the relation between the two quantities is rather due to the origin of both being the SOC. The key to understanding the MAE of a crystalline solid lies instead in the SOC and the details of the band structure near the Fermi energy, as revealed by Eq. 2.19.

Fig. 2.1 shows how the energy and orbital, as well as spin moments vary with the angle between the magnetisation direction and the  $z$ -direction as the magnetisation direction varies from  $[001]$  to  $[100]$ -direction, based on calculations done with WIEN2k. From Fig. 2.1b, which shows the change in energy plotted against the change in orbital moment, it is clear that there is a proportionality between these two quantities as predicted by Eq. 2.20 and that the easy axis of magnetisation coincides with direction where the orbital moment has its maximum. In Fig. 2.1c one can also observe that, as pointed out in references [23, 24], the largest change in orbital moment is on the Fe atom while that on the Ni atom is smaller and of opposite sign.

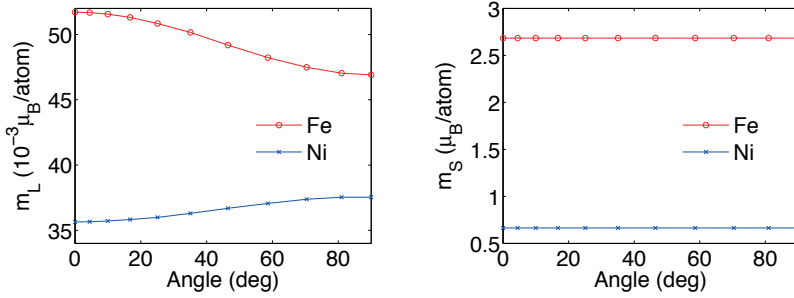
## 2.2 Exchange Interactions and the Heisenberg Hamiltonian

The quantised spin and orbital angular momentum and the associated magnetic moments allow us to understand the appearance of para- and diamagnetism. To understand spontaneous magnetic ordering, such as ferro-, ferri- or anti-ferromagnetism, we need to include also an interaction between the atomic magnetic moments. Interactions, such as dipole-dipole, between atomic moments are typically negligibly small and would not allow magnetic ordering at the significant temperatures where it is observed. The relevant interaction is instead the exchange interaction due to the Coulomb repulsion and the fermionic character of electrons. This can be seen, for example, in moving from Hartree to Hartree-Fock theory where the inclusion of antisymmetry of





(a) Change in total energy as function of angle between magnetisation direction and z-axis. (b) Change in energy versus change in orbital moment as angle is varied.



(c) Orbital moment as a function of angle. (d) Spin moment as a function of angle.

Figure 2.1. Variations in energy and moments of FeNi as functions of the angle  $\theta$  between the direction of magnetisation and the z-axis.

the wavefunction leads to an exchange term, which results in a lowering of energy for parallel spin ordering [15]. From, for example, the Heitler-London model one can see that localised spins tend to interact in a way so that the energy is proportional to the scalar product of the spin operators [16]. Even though the Heitler-London model only describes a simple system consisting of two atoms with one localised electron each, the result regarding the form of the spin-spin interaction turns out to be rather general and in many cases well describes also magnetism in a solid [15, 16]. This result is represented by the Heisenberg Hamiltonian

$$H_{\text{Heisenberg}} = -\frac{1}{2} \sum_{i \neq j} J_{ij} \mathbf{S}_i \cdot \mathbf{S}_j, \quad (2.21)$$

where  $\mathbf{S}_i$  and  $\mathbf{S}_j$  are the atomic spins on sites  $i$  and  $j$  respectively and  $J_{ij}$  is the exchange coupling parameter between these spins. For a magnetic system described by Eq. 2.21 the magnetic ordering and its  $T_C$  is now determined by the exchange coupling parameters  $J_{ij}$ . For a given material, these parameters can be obtained from the electronic structure as discussed in Sec. 3.1.5. Once

one has the  $J_{ij}$ , one can then study the magnetic ordering and transition temperatures via, for example, Monte Carlo simulations which will be discussed in Sec. 3.2. One can also estimate magnetic transition temperatures via mean field theory, according to which [15, 25]

$$T_C = \frac{J_0 S(S+1)}{3k_B}, \quad (2.22)$$

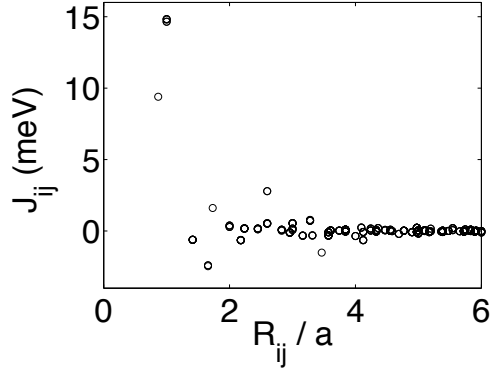
where  $S$  is the atomic spin,  $J_0 = \sum_i J_{0i}$  is the sum of the exchange interactions and  $k_B$  is the Boltzmann constant, from which it is clear that the Curie temperature is proportional to the strength of the exchange interactions. Eq. 2.22 overestimates the transition temperature by around twenty percent or more depending on dimensionality and coordination number [15], but can be useful in effortlessly establishing an upper limit for  $T_C$  and it is applied to some extent and compared with MC results in Paper III.

In ferromagnetic metals, which are the materials of main interest in this thesis, the exchange coupling tends to be mediated by conduction electrons and the coupling is said to be of RKKY-type. The typical form of the exchange coupling parameters in such a system is, asymptotically in the long range limit [25],

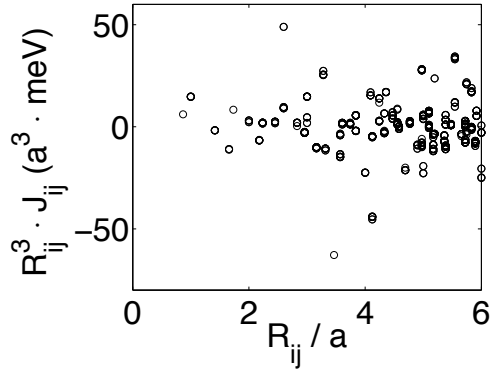
$$J_{ij}^{\text{RKKY}} \sim n^{4/3} \frac{\sin(2k_F R_{ij}) - 2k_F R_{ij} \cos(2k_F R_{ij})}{(k_F R_{ij})^4}, \quad (2.23)$$

where  $n$  is the density of conduction electrons,  $k_F$  is the Fermi wave vector and  $R_{ij}$  is the distance between sites  $i$  and  $j$ . Eq. 2.23 shows how RKKY-type interactions exhibit an oscillatory behaviour with a long range decay proportional to  $R_{ij}^{-3}$ . Strictly speaking, Eq. 2.23 is derived assuming localised moments in a metal and only in this type of system one can formally expect the Heisenberg Hamiltonian with exchange coupling parameters given by Eq. 2.23 to be a good model. Hence, one would not expect the model to work for magnetic 3d metals as these tend to exhibit itinerant ferromagnetism with an exchange splitting of the conduction bands. However, it turns out that the same type of behaviour is often found also in itinerant ferromagnets [26, 27].

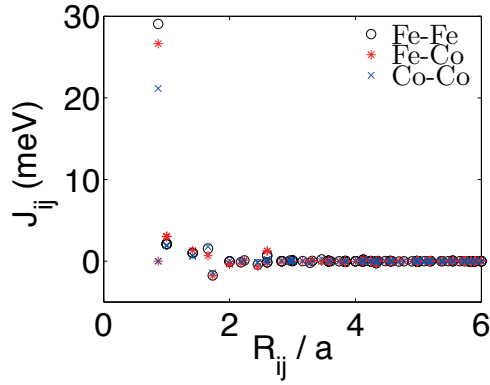
Fig. 2.2 illustrates the exchange coupling parameters for Fe and random alloy  $\text{Fe}_{0.4}\text{Co}_{0.6}$  in the bcc structure, calculated by the SPR-KKR method which is described in the next chapter. Fig. 2.2b illustrates that the exchange coupling parameters decay approximately as  $R_{ij}^{-3}$ , as expected from Eq. 2.23. In Fig. 2.2c it is seen that the strength of the Fe-Fe interactions increase as Co is alloyed into the material while also Fe-Co and Co-Co interactions are very strong. This explains the observed effect that  $T_C$  increases as one alloys Co into bcc Fe [28] and application of mean field theory on the exchange coupling parameters in Fig. 2.2 results in  $T_C = 1298$  K and  $T_C = 1554$  K for Fe and  $\text{Fe}_{0.4}\text{Co}_{0.6}$  respectively. Looking at Eq. 2.23 it can be speculated that the increase in the strength of the  $J_{ij}$  is due to an increase in the density of conduction electrons as Co is added into the material.



(a) bcc Fe



(b) bcc Fe



(c) bcc Fe<sub>0.4</sub>Co<sub>0.6</sub>

Figure 2.2. Exchange coupling parameters,  $J_{ij}$ , for bcc Fe and bcc Fe<sub>0.4</sub>Co<sub>0.6</sub>, as a function of interatomic distances. 2.2b shows  $J_{ij} \cdot R_{ij}^3$  to illustrate the RKKY-type long-range behavior of exchange interactions in bcc Fe.

The Hamiltonian in Eq. 2.21 is rotationally invariant and hence does not include any form of magnetic anisotropy. The Heisenberg Hamiltonian can be expanded with a term to take into account magnetocrystalline anisotropy and in the case of a uniaxial crystal, based on Eq. 2.16 if one keeps only the two first anisotropy constants, such a Hamiltonian is

$$H_{\text{MAE}} = \sum_i \left[ K_1 (\hat{\mathbf{m}}_i \cdot \hat{\mathbf{e}}_z)^2 + K_2 (\hat{\mathbf{m}}_i \cdot \hat{\mathbf{e}}_z)^4 \right], \quad (2.24)$$

where  $\hat{\mathbf{m}}_i$  is the direction of the moment at site  $i$  and  $\hat{\mathbf{e}}_z$  is the direction of the crystal axis.

### 3. Computational Methods

This chapter provides a brief description of the computational methods utilised in the work behind this thesis. Density functional theory (DFT) [29, 30, 31] is used to calculate ground state properties of materials and it is described in Sec. 3.1. In particular the full potential linearised augmented plane waves and the spin polarised relativistic KKR methods are used to solve the DFT equations and an introduction to these methods is given in Sec 3.1.1 and Sec. 3.1.2. As we are interested in disordered alloys, models to describe these are discussed in Sec. 3.1.3 while Sec. 3.1.4 provides a discussion on specifics regarding the computation of MAE. In order to calculate Curie temperatures, Monte Carlo simulations [32] are employed as discussed in Sec. 3.2.

#### 3.1 Density Functional Theory

Density functional theory (DFT) is our method of choice for finding the ground state solution to an  $N$ -electron Schrödinger equation of the form

$$\left( -\frac{\hbar^2}{2m} \sum_{i=1}^N \nabla_i^2 + \sum_i V_{\text{ext}}(\mathbf{r}_i) + \frac{1}{2} \sum_{i \neq j}^N w(|\mathbf{r}_i - \mathbf{r}_j|) \right) \Psi = E\Psi, \quad (3.1)$$

where  $V_{\text{ext}}(\mathbf{r})$  is an external potential,  $w(|\mathbf{r}_i - \mathbf{r}_j|)$  is a Coulomb interaction between an electron at  $\mathbf{r}_i$  and one at  $\mathbf{r}_j$  and  $\Psi$  is an  $N$ -electron wavefunction. The first key ingredients of DFT are the Hohenberg-Kohn theorems [33] which allow us to focus on electron densities, rather than wavefunctions, and finding the ground state properties of the system by minimising the total energy as a functional with respect to the density. The practical method of doing this is provided by the Kohn-Sham approach[34] where the many-body problem in Eq. 3.1 is simplified to a number of single particle problems

$$\left( -\frac{\hbar^2}{2m} \nabla^2 + V_{\text{eff}}(\mathbf{r}) \right) \psi_i(\mathbf{r}) = \epsilon_i \psi_i(\mathbf{r}), \quad (3.2)$$

where  $\epsilon_i$  and  $\psi_i$  are the Kohn-Sham eigenvalues and orbitals which, in general, individually lack clear physical interpretation, although the ground state density is

$$n(\mathbf{r}) = \sum_i^N |\psi_i(\mathbf{r})|^2, \quad (3.3)$$

with summation over the  $N$  eigenstates with lowest energy. In making this simplification, we have introduced the effective single particle potential

$$V_{\text{eff}}(\mathbf{r}) = V_{\text{ext}}(\mathbf{r}) + \int d\mathbf{r}' \frac{n(\mathbf{r})}{|\mathbf{r} - \mathbf{r}'|} + \frac{\delta E_{\text{xc}}[n(\mathbf{r})]}{\delta n(\mathbf{r})}, \quad (3.4)$$

including the exchange-correlation potential  $V_{\text{xc}} = \frac{\delta E_{\text{xc}}[n(\mathbf{r})]}{\delta n(\mathbf{r})}$ , which contains the many-body effects. This unknown quantity,  $V_{\text{xc}}$ , is the cost of our simplification from a many-electron wavefunction into single particle problems and finding good approximations for  $V_{\text{xc}}$  is the grand challenge in making DFT accurate and useful. For some very simple model systems it might be possible to find an exact exchange-correlation functional [35] but realistic systems must be treated by approximations. The most commonly used approximations for the exchange-correlation potential are the local density approximation [36, 37] (LDA), which locally approximates the  $V_{\text{xc}}(\mathbf{r})$  with that of a homogeneous electron gas with the same density  $n(\mathbf{r})$ , and the generalised gradient approximation [38] (GGA), which also takes into account gradients in the density. For many systems, these approximations are sufficient to reproduce ground state properties with satisfying accuracy although for so called strongly correlated systems other corrections, such as LDA+ $U$  [29, 30] or dynamical mean field theory (DMFT) [39, 30], are required.

In this thesis, we are mainly interested in the magnetic properties of 3d metals and their alloys and compounds. For these systems GGA tends to accurately describe the desired properties [40, 41, 42], whereby this is the main exchange-correlation potential employed in the calculations behind this work.

In the discussion above no spin dependence was included. In order to describe magnetism, spin polarised DFT must be used. The density should then be split up into spin up and spin down parts so  $n(\mathbf{r}) = n_{\uparrow}(\mathbf{r}) + n_{\downarrow}(\mathbf{r})$  and spin dependence should be included into the effective potential. Furthermore, as discussed in Sec. 2.1, relativistic effects are often important and can be taken into account, for example by solving the Dirac equation rather than the Schrödinger equation or by using the scalar relativistic approximation discussed in Sec. 2.1.1. In particular, spin-orbit coupling is essential for calculating magnetocrystalline anisotropy and specifics regarding this will be discussed in Sec. 3.1.4.

The next step in DFT is to solve the equations in Eq. 3.2. Many methods have been developed for doing this and, as usual in numerical problem solving, one typically needs to weigh computational speed against accuracy and generality. Those methods of solving the Kohn-Sham equations which are used in the work behind this thesis will be briefly described in the coming two sections. Since the density, which is calculated from the solutions  $\psi_i$ , is also needed to calculate the potential  $V_{\text{eff}}$  which appears in the equations, the problem is solved self-consistently by iteration until a solution is converged with required accuracy.

### 3.1.1 FP-LAPW

One of the computational methods used here is the full potential linearised augmented plane waves [43] (FP-LAPW) method as implemented in the WIEN2k code [44]. Full potential implies that no shape approximation is applied for the potential, in contrast to the commonly used atomic sphere approximation (ASA), where the potentials are assumed to be spherically symmetric around atoms. LAPW is the linearised[45] version of Slater's augmented plane wave [46] (APW) method, in the sense that energy dependence is removed from the basis functions. Space is partitioned into muffin-tin (MT) regions of atomic spheres  $S_\alpha$  and an interstitial region  $I$ , whereupon the Kohn-Sham orbitals in Eq. 3.2 are expanded in basis functions consisting of radial solutions  $u_l^\alpha(r', E_l^\alpha)$  to the Schrödinger equation of a free atom with energy  $E_l^\alpha$  and its energy derivative  $\dot{u}_l^\alpha(r', E_l^\alpha)$  within  $S_\alpha$ , while in  $I$ , plane waves are used according to

$$\phi_{\mathbf{k}, \mathbf{K}}(\mathbf{r}) = \begin{cases} \frac{1}{\sqrt{V}} e^{i(\mathbf{k}+\mathbf{K}) \cdot \mathbf{r}} & \mathbf{r} \in I \\ \sum_{l,m} \left( A_{l,m}^{\alpha, \mathbf{k}+\mathbf{K}} u_l^\alpha(r', E_l^\alpha) + B_{l,m}^{\alpha, \mathbf{k}+\mathbf{K}} \dot{u}_l^\alpha(r', E_l^\alpha) \right) Y_m^l(\hat{\mathbf{r}}') & \mathbf{r} \in S_\alpha \end{cases} \quad (3.5)$$

Here  $\mathbf{k}$  is a point in the Brillouin zone,  $\mathbf{K}$  is a reciprocal lattice vector,  $V$  is the volume of the unit cell,  $Y_m^l(\hat{\mathbf{r}}')$  are spherical harmonics and  $\mathbf{r}'$  is the position relative to the position coordinate of atomic sphere  $S_\alpha$ . On the boundary of the atomic spheres a matching is done so that  $\phi_{\mathbf{k}, \mathbf{K}}(\mathbf{r})$  is continuous and differentiable in all space. The number of basis functions used are usually determined so that one basis vector is included for each vector  $\mathbf{K}$  such that  $|\mathbf{K}| < K_{\max}$  with  $R_{\text{MT}} K_{\max} = \text{convergence parameter}$ , where  $R_{\text{MT}}$  is the radius of the smallest atomic sphere. The Kohn-Sham equations can then be solved as an eigenvalue problem for a dense enough grid of  $\mathbf{k}$ -vectors to obtain an accurate solution to the problem.  $R_{\text{MT}} K_{\max}$  is a good parameter to describe the accuracy of the number of basis functions used since smaller radii of atomic sphere will require more basis functions to be included to describe the more rapid real space variations closer to the nuclei.

In the WIEN2k code, core state electrons are treated fully relativistically by solving the spherically symmetric Dirac equation, while valence states in atomic spheres are treated within the scalar relativistic approximation discussed in Sec. 2.1.1. In order to calculate MAE, one needs to include the SOC also for valence states which can be done in a second variational approach [47, 48].

### 3.1.2 SPR-KKR

As in the previously discussed scheme, the spin-polarised relativistic Korringa-Kohn-Rohstocker method [49, 50] relies on simplifying the many-body Schrödinger equation to a number of single particle Kohn-Sham equations. This method

goes back to the work of Korringa [51] and Kohn and Rohstocker [51] (KKR) and allows for exact solutions to an MT potential which is spherically symmetric around atoms and constant in the interstitial region. The SPR-KKR method evaluates the Green's function [52] (GF),  $G(\mathbf{r}, \mathbf{r}', E)$ , defined according to

$$(E - \mathcal{H})G(\mathbf{r}, \mathbf{r}', E) = \delta(\mathbf{r} - \mathbf{r}'), \quad (3.6)$$

where  $\mathcal{H}$  is the Hamiltonian of the system. With a free electron GF  $G^0(\mathbf{r}, \mathbf{r}', E)$ , the single-site GF can be introduced via a Dyson equation

$$G^n(\mathbf{r}, \mathbf{r}', E) = G^0(\mathbf{r}, \mathbf{r}', E) + G^0(\mathbf{r}, \mathbf{r}', E)t_n G^0(\mathbf{r}, \mathbf{r}', E), \quad (3.7)$$

where  $t_n$  is the single site  $t$ -matrix. In SPR-KKR, the full GF is then evaluated through a multiple-scattering formalism [50, 53] so that

$$G(\mathbf{r}, \mathbf{r}', E) = G^0(\mathbf{r}, \mathbf{r}', E) + G^0(\mathbf{r}, \mathbf{r}', E)T G^0(\mathbf{r}, \mathbf{r}', E), \quad (3.8)$$

where

$$T = \sum_{n, n'} \tau_{nn'} \quad (3.9)$$

and  $\tau_{nn'}$  is the scattering path operator which brings an incoming electron at site  $n$  to an outgoing at site  $n'$ . For a crystal these may be evaluated via Lloyd's formula [50, 53].

The method outlined above allows for evaluation of the energy dispersion relation  $E(\mathbf{k})$ . For a disordered crystal, which will be further discussed in the coming section, the ordinary dispersion relation is, however, not well defined. Instead one can evaluate the more general Bloch spectral functions [54, 50],  $A(E, \mathbf{k})$ , an example of which will be provided in Fig. 3.3. For an ordered crystal these reduce to the ordinary dispersion relations.

### 3.1.3 Models to Treat Disorder

We will be interested in studying randomly disordered alloys where, for example, one might be interested in the magnetic properties of  $\text{Fe}_{1-x}\text{Co}_x$  as a function of the concentration  $x$ . Hence, we need models to describe this type of disorder and there are various methods available[55]. In super cell calculations, one creates a large system with many atoms and by means of some appropriate stochastic method, such as special quasirandom structures (SQS) [56], places the desired concentration of atoms in an appropriate configuration and evaluates the electronic structure. This should often be the most accurate model, in particular as it keeps the specific atomic character of each atom and correctly allows for local relaxation, but it quickly becomes computationally demanding and does not allow one to easily vary the concentration in small increments. Two other models, namely virtual crystal approximation (VCA) and the coherent potential approximation (CPA) are therefore utilised to great extent in this



thesis and will be discussed in more detail. Some comparison to SQS super cell calculations can be found in Paper I.

VCA is a single site approach and perhaps one of the simplest methods which can be used. Here one introduces a virtual atom C to describe the binary alloy  $A_{1-x}B_x$  and this virtual atom should have a possibly non-integer atomic number  $Z_C = (1-x)Z_A + xZ_B$ . This simple model has been confirmed to yield a correct behaviour for various properties when alloying elements such as Fe and Co, which are neighbours in the periodic table, while it breaks down for elements further away from each other, such as Fe and Ni [57, 58]. Alternatively formulated, the potential

$$V_C = (1-x)V_A + xV_B \quad (3.10)$$

yields a correct description of the random alloy consisting of atoms A and B with potentials  $V_A$  and  $V_B$  respectively in the limit where  $V_A = V_B$  [55]. However, the MAE which is one of the key properties studied in this thesis, tends to be quantitatively severely overestimated by VCA, even when the qualitative behaviour is correct [59, 60]. This is highly relevant for Papers I and II where it is also discussed.

A more sophisticated single site model of disorder is provided by the CPA [61]. Here, an impurity of each atom type, A or B, is placed in an effective CPA medium. One then considers the alloy to be described by the weighted average of the two different impurity solutions, as illustrated in Fig. 3.1. This method is suitable for use with the GF approach where one solves the CPA equations

$$(1-x)\tau_{nn}^A + x\tau_{nn}^B = \tau_{nn}^{\text{CPA}} \quad (3.11)$$

and

$$\tau_{nn}^\alpha = [(t^\alpha)^{-1} - (t^{\text{CPA}})^{-1} - (\tau^{\text{CPA}})^{-1}]^{-1}, \quad \alpha = A, B, \quad (3.12)$$

self consistently, whereupon an average GF,

$$G(\mathbf{r}, \mathbf{r}', E) = (1-x)G^A(\mathbf{r}, \mathbf{r}', E) + xG^B(\mathbf{r}, \mathbf{r}', E), \quad (3.13)$$

is obtained.

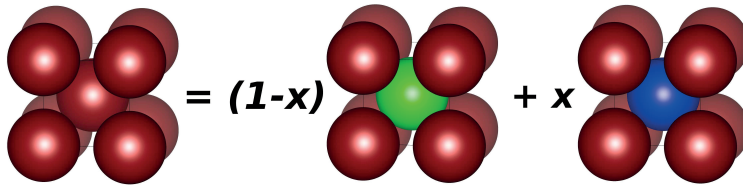


Figure 3.1. In the CPA, each atomic type is embedded in an effective CPA medium and the average solution is used.

Fig. 3.2 shows a comparison between a VCA calculation in WIEN2k and a CPA calculation using SPR-KKR. The MAE and magnetic moments have

been calculated as functions of the tetragonal strain  $c/a$  for an alloy of  $\text{Fe}_{0.4}\text{Co}_{0.6}$ , similarly as has been done in Ref. [59]. The MAE has been evaluated by total energy difference and magnetic force theorem in WIEN2k and with total energy difference and the torque method in SPR-KKR. These methods of computing the MAE will be described in the coming section 3.1.4. Fig. 3.2a illustrates

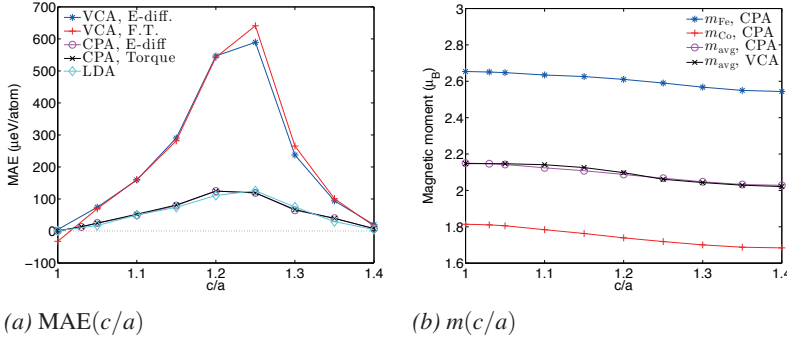


Figure 3.2. MAE and magnetic moments of  $\text{Fe}_{0.4}\text{Co}_{0.6}$  as functions of  $c/a$ , calculated by various methods. All calculations were done with the exchange-correlation treated with the GGA, except the MAE calculation marked LDA, which was performed with SPR-KKR, CPA and total energy difference calculation.

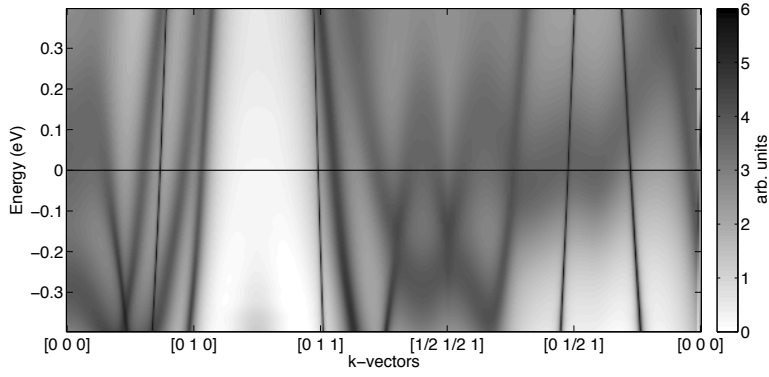
how the VCA qualitatively describes the correct behaviour of the MAE, although it overestimates the maximum values significantly compared to the CPA. From Fig. 3.2b it is clear that the moment provided by the VCA coincides very well with the average moment provided by CPA, but CPA yields more information as it also provides the atom specific moments, not only the average.

Fig. 3.3 illustrates the Bloch spectral functions around the Fermi energy for the disordered tetragonal alloy  $\text{Fe}_{0.4}\text{Co}_{0.6}$  with three different tetragonal strains around that of  $c/a = 1.2$ , with maximum MAE as was found in Fig. 3.2. It can be observed how there are regions with occupied and unoccupied energy bands getting particularly close to the  $E_F$  for  $c/a = 1.2$  and based on the discussion in Sec. 2.1.2 one can hypothesise that this is the reason for the large MAE.

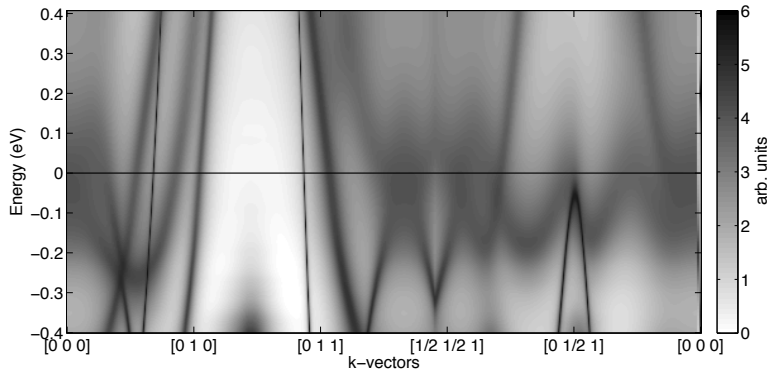
### 3.1.4 Computing the MAE

When defining the MAE as the largest possible energy difference between two different magnetisation directions (the easy and the hard axes), it is clear that this can be calculated by performing total energy calculations, including SOC, for a magnetisation in each of the two directions  $\hat{\mathbf{n}}_1$  and  $\hat{\mathbf{n}}_2$  and taking the difference according to

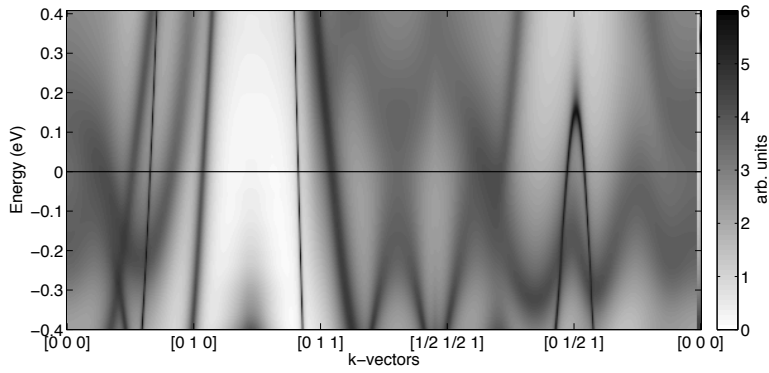
$$E_{\text{MAE}} = E(\hat{\mathbf{n}}_1) - E(\hat{\mathbf{n}}_2). \quad (3.14)$$



(a)  $c/a = 1.15$ , MAE =  $79.3 \mu\text{eV}/\text{atom}$



(b)  $c/a = 1.2$ , MAE =  $124.6 \mu\text{eV}/\text{atom}$



(c)  $c/a = 1.25$ , MAE =  $118.9 \mu\text{eV}/\text{atom}$

**Figure 3.3.** Bloch spectral functions around the Fermi energy for bct  $\text{Fe}_{0.4}\text{Co}_{0.6}$  with various tetragonal strains.

The first problem here is determining which axis is easy and which is hard when there is infinitely many directions to probe. This however, does not tend to be a problem since the directions of interest are typically some of the high symmetry directions which can be seen in the phenomenological expressions in Sec. 2.1.2. Furthermore, in a uniaxial crystal, it is typically enough to probe the energy in the uniaxial direction and in one arbitrary direction in the orthogonal plane as energy variations within the plane tend to be orders of magnitude smaller. For example, in the tetragonal  $\text{Fe}_{0.4}\text{Co}_{0.6}$  alloy with  $c/a = 1.2$ , the energy difference between magnetisation directions along  $z$ -axis or in the  $xy$ -plane is  $\text{MAE} = 1.2 \cdot 10^{-4} \text{ eV/atom}$ , while the energy variations within the plane are too small to be resolved with a numerical accuracy of  $10^{-8} \text{ Ry/atom} = 1.36 \cdot 10^{-7} \text{ eV/atom}$ . What is on the other hand a problem is that the MAE tends to be a very small energy difference, compared to for example exchange interactions, which are still only in the order of a few  $\text{meV/atom}$ . Hence, one is required to compute a small difference between two large energy values and this makes the MAE difficult to evaluate with high numerical accuracy and thus also computationally costly. Fig. 3.4 shows the convergence of the MAE as a function of the number of  $\mathbf{k}$ -points used in integration over the Brillouin zone. This is evaluated as the difference of total energies for FeNi, one of the materials studied in Paper III. The calculation is done using WIEN2k where the Brillouin zone integration is performed with the modified tetrahedron method[62]. It is clear that, at least, more than  $10^4$   $\mathbf{k}$ -points should be sampled over the full Brillouin zone in order to obtain a value of the MAE with numerical accuracy within a few percent.

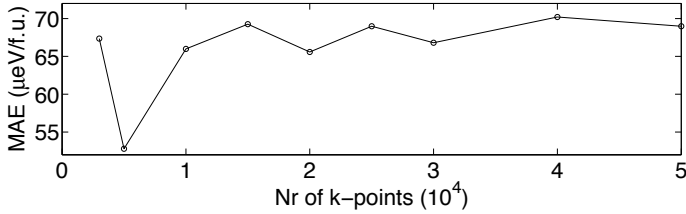


Figure 3.4. MAE as a function of the number of  $\mathbf{k}$ -points used for numerical integration of the Brillouin zone for  $L1_0$  structured alloy FeNi.

Approximative methods have been developed to evaluate the MAE from DFT with greater ease and less computational cost. Two such methods, which have been utilised in this work and will be described here, are the force theorem used in Papers I and II and the torque method which is used to a large extent in Paper III.

### Force Theorem

When calculating the MAE as a difference of total energies as described above, one needs to perform highly accurate, full self consistent calculations, includ-

ing SOC, in each of the two magnetisation directions. By considering the change in energy within first order perturbation theory, the magnetic force theorem[63] tells us that it is enough to consider the change in the single particle Kohn-Sham eigenvalues, rather than the total energy. The MAE can then be evaluated as [64]

$$E_{\text{MAE}} \approx E_{\text{s.p.}}(\hat{\mathbf{n}}_1) - E_{\text{s.p.}}(\hat{\mathbf{n}}_2), \quad (3.15)$$

where

$$E_{\text{s.p.}} = \sum_{\text{occ. } i} \varepsilon_i \quad (3.16)$$

is the sum over occupied single particle Kohn-Sham energy eigenvalues. This allows running only one full self consistent calculation and evaluating the  $\varepsilon_i$ , including SOC, for each magnetisation direction, saving about half of the computational effort. Fig. 3.2 contains a comparison of the MAE calculated by total energy difference or using the force theorem and illustrates that, within the VCA, the force theorem provides a good approximation of the MAE for the given system.

### Torque Method

Another method for calculating the MAE, implemented in SPR-KKR and employed to considerable extent in Paper III, is the torque method[65]. For a uniaxial magnet, considering the first two  $\theta$ -dependent terms in Eq. 2.16, one finds that the torque on a magnetic moment in direction  $(\sin \theta \cos \phi, \sin \theta \sin \phi, \cos \theta)$  is

$$T(\theta) = \frac{dE}{d\theta} = K_1 \sin 2\theta + 2K_2 \sin^2 \theta \sin 2\theta. \quad (3.17)$$

From Eq. 3.17 it is easy to evaluate the MAE as

$$E_{\text{MAE}} = T\left(\frac{\pi}{4}\right) = K_1 + K_2 = E(0) - E\left(\frac{\pi}{2}\right), \quad (3.18)$$

if a method to evaluate torque is available. In the multiple scattering formalism adopted in SPR-KKR, the torque can be obtained through the formula [66]

$$T(\theta) = -\frac{1}{\pi} \text{Im} \int^{\varepsilon_F} d\varepsilon \sum_n \text{Tr} \left( \frac{\partial t_n^{-1}}{\partial \theta} \tau_{mn}(\varepsilon) \right). \quad (3.19)$$

Fig. 3.2 contains a comparison between torque method calculations and total energy difference calculations for the MAE of  $\text{Fe}_{0.4}\text{Co}_{0.6}$  as a function of  $c/a$  and the agreement is excellent. In the work behind Paper I on the other hand, the torque method was found to not describe the MAE of C-doped FeCo alloys well, most likely due to the local disorder introduced by the C-atom.

### 3.1.5 Exchange Coupling Parameters

The exchange coupling parameters  $J_{ij}$  of the Heisenberg Hamiltonian discussed in Sec. 2.2 can, within KKR multiple scattering formalism, be evaluated via the formula of Liechtenstein *et al.* [67, 68] as

$$J_{ij} = -\frac{1}{4\pi} \text{Im} \int^{\epsilon_F} d\epsilon \text{Tr} \left[ (t_{i\uparrow}^{-1} - t_{i\downarrow}^{-1}) \tau_{\uparrow}^{ij} (t_{j\uparrow}^{-1} - t_{j\downarrow}^{-1}) \tau_{\downarrow}^{ji} \right]. \quad (3.20)$$

Calculation of exchange coupling parameters via Eq. 3.20 is implemented in SPR-KKR and the result of such a calculation was shown in Fig. 2.2. With these  $J_{ij}$  as input, one can model finite temperature effects in various ways including mean field theory, Monte Carlo simulations or spin dynamics based on the Landau-Lifshitz-Gilbert equation [69]. The main method used in this work and in Paper III in particular is Monte Carlo simulations which will be discussed further in the coming section.

## 3.2 Monte Carlo Simulations

In statistical mechanics [70] one wishes to evaluate partition functions

$$Z = \text{Tr} e^{-H/k_B T} \quad (3.21)$$

and expectation values such as

$$\langle A \rangle = \frac{1}{Z} \text{Tr} A e^{-H/k_B T}. \quad (3.22)$$

Calculating these traces for complicated systems, containing many particles, amounts to evaluating sums or integrals over a phase space with a large number of dimensions. This soon becomes insurmountable with deterministic methods but it turns out that stochastic methods such as Monte Carlo (MC) [71, 32] simulations, which calculate averages from large sets of random numbers, are well suited to solve these problems. In general MC allows for efficient evaluation of multidimensional integrals, as an integral may be considered an expectation value of a probability distribution, and is often more efficient than deterministic methods in more than three dimensions [71]. When it comes to solving the problems of classical statistical mechanics, the algorithm of Metropolis *et al.* [72] provides a powerful method of solution.

Here, we are mainly interested in the Heisenberg Hamiltonian in Eq. 2.21. The state of such a system is described by the directions of all the  $N$  spins in the system, i.e. the set  $\{\hat{\mathbf{m}}_i\}$ . The average moment of a particular configuration is  $\mathbf{m} = \frac{1}{N} \sum_i \mathbf{m}_i$  and the energy  $E(\{\hat{\mathbf{m}}_i\})$  is easily calculated from Eq. 2.21. By generating many different states based on random numbers one can evaluate thermodynamic averages such as average energy per spin  $e = \langle H \rangle / N$ , specific heat capacity

$$c = \frac{\partial e}{\partial T} = \frac{\langle H^2 \rangle - \langle H \rangle^2}{NT^2} \quad (3.23)$$

or magnetic susceptibility

$$\chi = \frac{\partial m}{\partial h} = \frac{\langle m^2 \rangle - \langle m \rangle^2}{NT}, \quad (3.24)$$

where  $h$  is an applied field.

The Metropolis algorithm applied on this type of system can be summarised as follows:

1. Generate an appropriate initial configuration, e.g., random or all spins aligned.
2. For each  $i$ , randomly generate a new trial state where  $\hat{\mathbf{m}}_i$  is changed to  $\hat{\mathbf{m}}'_i$  and calculate the change in energy  $\Delta E$ . Generate a uniformly distributed random number  $r \in [0, 1]$  and accept the new trial state if  $r < e^{-\Delta E/k_B T}$ , otherwise keep the old state as the new state. To do this for each of the  $N$  spins is known as one MC sweep.
3. Repeat the second step and after every other sweep measure wanted quantities and evaluate thermodynamic averages. Repeat the procedure for a large enough number of sweeps so that the averages are well converged.

Before taking measurements one should run a number of sweeps to make the system unbiased from the initial state and often it is also good to do a simulated annealing where the temperature is slowly lowered to the measurement temperature from a higher temperature in order to stop the system from being trapped in a local energy minimum [32].

In practice when performing simulations one is limited to particle numbers which are very small compared to the sizes of real systems with  $\sim 10^{23}$  particles. Recurrently, one might wish to analyse system properties in the thermodynamic limit, i.e., where the size of the system goes to infinity under constant density, which can be done using the methods of finite size scaling. Critical points can be analysed using critical exponents and the Binder cumulant method [71, 32]. One is then interested in the Binder cumulant,

$$U = 1 - \frac{\langle m^4 \rangle}{\langle m^2 \rangle^2}, \quad (3.25)$$

which is independent of system size at the critical point where a second order phase transition occurs. Hence, plotting this quantity as a function of a thermodynamic variable, such as temperature, for various system sizes and finding the point of intersection allows one to identify the critical point in the thermodynamic limit.

Figure 3.5 shows the average moment and the magnetic susceptibility as functions of temperature for L1<sub>0</sub> alloy FeNi with various system sizes described by  $L$  so that there is a total  $L^3$  unit cells included in the simulation. The particular MC implementation used here and in the work behind Paper III is that of the UppASD code [69]. In Fig. 3.5a one can observe how the average moment decreases with temperature and how it decreases particularly fast

close to the transition temperature of  $T_C = 916$  K. One can also see that for larger  $L$ , the drop in the moment is steeper and the value above  $T_C$  goes closer to the value of zero which is expected in the thermodynamic limit. In Fig. 3.5b it is shown how the susceptibility diverges at the critical point and the peak becomes sharper for larger  $L$ . A fast and easy way to identify the point of the phase transition is to look for peaks in the susceptibility. Fig. 3.6 shows the

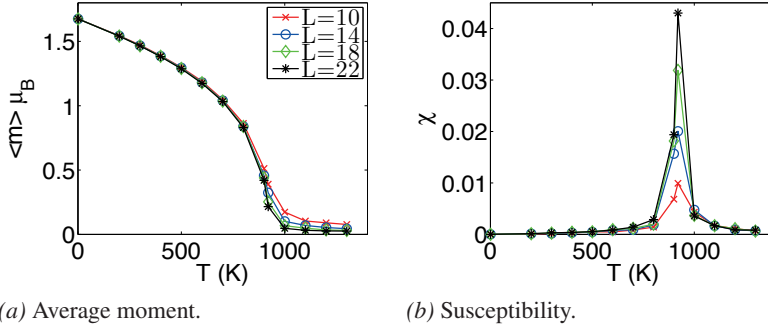


Figure 3.5. Average moment and magnetic susceptibility as functions of temperature for L1<sub>0</sub> alloy FeNi with system sizes  $L$ .

Binder cumulant as function of temperature for the FeNi systems of size  $L$ . The inset shows a close-up of the region around the critical point where one can see how the curves for different  $L$  intersect at  $T_C$ .

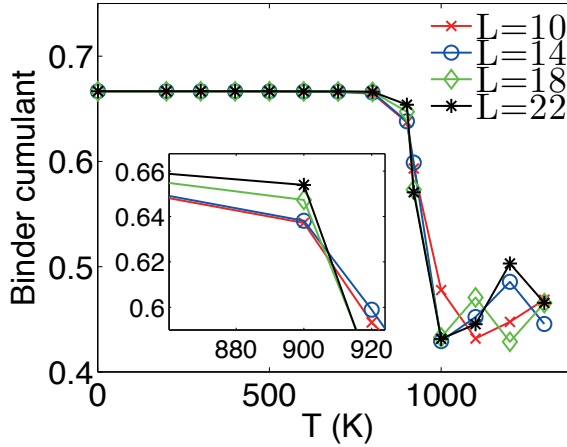


Figure 3.6. Binder cumulant as a function of temperature for L1<sub>0</sub> alloy FeNi with system sizes  $L$ .



## 4. Results

This chapter presents a brief overview of the key results of this thesis, while readers interested in more details are referred to the papers. First, a general discussion on FeCo alloys is provided in Sec. 4.1 and results regarding FeCo alloys with C impurities, related to the work in papers I and II, are presented in Sec. 4.1.1. The possibility of using B instead of C is discussed in Sec. 4.1.2. In Sec. 4.2 results regarding binary alloys in the  $L1_0$  structure, based on the work in paper III, are presented. Finally a number of other interesting materials are briefly discussed.

### 4.1 $\text{Fe}_{1-x}\text{Co}_x$ Alloys

As  $\text{Fe}_{1-x}\text{Co}_x$  alloys provide large saturation magnetisation, being on top of the Slater-Pauling curve [73, 8], as well as high Curie temperature, they would be ideal candidates for permanent magnet applications if a large MAE can be obtained as well. Burkert *et al.* [18] showed that an enormous MAE could be obtained in tetragonally strained  $\text{Fe}_{1-x}\text{Co}_x$  given specific conditions of  $c/a \approx 1.2$  and  $x \approx 0.65$ . The work of Burkert *et al.* was based on the VCA and as seen in Sec. 3.1.3 it overestimates the MAE, but more realistic CPA or supercell treatment of disorder showed that indeed large MAE can be obtained even if maximum values are smaller than those originally proposed by Burkert *et al.* [59, 60]. These theoretically predicted results were also experimentally verified in thin film multilayers [74, 75, 76]. Unfortunately, most of the Fe-Co phase diagram below 1100 K is bcc [77] and exhibits a minute MAE so in order to produce bulk magnets based on  $\text{Fe}_{1-x}\text{Co}_x$  for permanent magnets new routes must be explored. Papers I and II provide such a new route by introducing doping with C atoms which cause a tetragonal strain of the  $\text{Fe}_{1-x}\text{Co}_x$  crystal as will be discussed in the coming Section 4.1.1. If this route is possible with C atoms, one can also imagine using other similar atoms, such as B or N, out of which B will be discussed in Sec. 4.1.2.

Pure Co is found in the uniaxial hcp structure at normal conditions, which allows it to have a significantly higher MAE compared to bcc Fe. Another possible system to explore could hence be  $\text{Fe}_{1-x}\text{Co}_x$  in the hcp structure. The first apparent problem with this system is that hcp is only the stable phase for a very narrow range of  $x \sim 1$  [77]. However, FP-LAPW simulations were still performed to explore the magnetic properties of the hypothetical hcp  $\text{Fe}_{1-x}\text{Co}_x$  system for a complete range of  $x \in [0, 1]$ , also varying the lattice

parameters around their equilibrium values. It is found that very large values of  $E_{\text{MAE}} > 400 \mu\text{eV}/\text{atom}$  are obtained for  $x \sim 0.3$  or smaller, but the system also appears to be antiferromagnetic for  $x \geq 0.5$  so that no magnetisation would be left, making the system unsuitable as a permanent magnet even if one would manage to alloy large amounts of Fe into the hcp crystal.

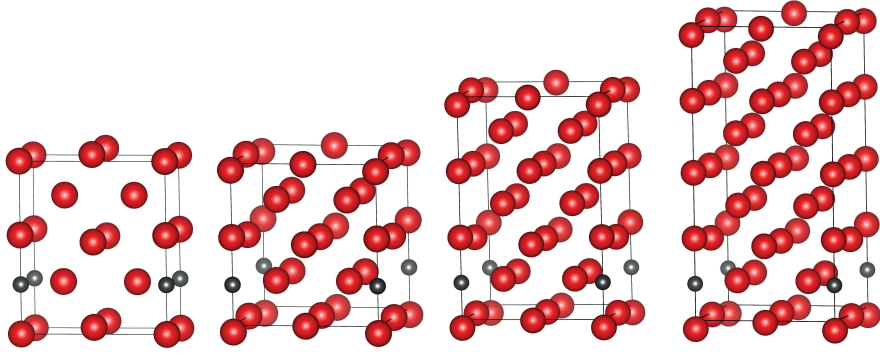
#### 4.1.1 $(\text{Fe}_{1-x}\text{Co}_x)\text{-C}$

The metastable Fe-C martensite phase is an old and well known system where C atoms go into octahedral interstitial positions of the bcc Fe crystal, where they cause a tetragonal distortion [78, 79, 80]. This metastable phase is practically obtained by rapid quenching of the high temperature fcc phase. Due to similarities in the phase diagrams of Fe-C and Fe-Co-C systems [77, 81], it is reasonable to imagine the same type of structure occurring in an alloy of  $\text{Fe}_{1-x}\text{Co}_x\text{-C}$ . This would allow one to produce a tetragonal  $\text{Fe}_{1-x}\text{Co}_x$  based system potentially possessing the desired permanent magnet properties, including a large MAE, if the desired conditions of  $c/a \approx 1.2$  and  $x \approx 0.65$  pointed out in Ref. [18] can be achieved.

In Paper I, stable energy minima with  $c/a > 1$  are presented for a number of internally relaxed  $(\text{Fe}_{1-x}\text{Co}_x)_y\text{C}$  systems with  $y = 8, 16$  and  $24$  and C in octahedral interstitial positions as illustrated in Fig. 4.1a-4.1c and a few different values of  $x$  around  $0.65$  as suggested by Ref. [18]. This indicates that it could indeed be possible to find the desired type of martensite structures described above. For systems with  $y = 16$ , relatively large tetragonal strains up to  $c/a \approx 1.17$  are found so that potentially large values of the MAE can be obtained. For systems with a lower C content, i.e.  $y = 24$ , the strain is significantly lower and  $c/a \approx 1.035$ .

For each of these systems the MAE, is calculated by both WIEN2k with VCA and the force theorem and by SPR-KKR with CPA and total energy differences. As expected, the VCA calculations overestimate the MAE significantly, but even with the CPA significant MAE's of up to  $E_{\text{MAE}} = 41.6 \mu\text{eV}/\text{atom} = 0.59 \text{ MJ}/\text{m}^3$  are found. Supercell calculations, utilising special quasirandom structures (SQS), provide an even slightly larger value of  $E_{\text{MAE}} = 0.75 \text{ MJ}/\text{m}^3$ . These systems also exhibit large saturation magnetisations of  $\mu_0 M_S \approx 2 \text{ T}$  and if one might guess that a small amount of non-magnetic C does not drastically affect the strong exchange interactions of Fe and Co atoms, it is reasonable to suspect also a significant Curie temperature, which in summary makes the system highly promising as a permanent magnet if possible to synthesise.

These results provide a potential route to a new permanent magnet but thus far all results are theoretical suggestions and the next step should be an experimental confirmation. Such a confirmation is provided in Paper II, where pulsed laser deposition is used for epitaxial growth of the  $(\text{Fe}_{1-x}\text{Co}_x)_y\text{C}$  system described above. It is found that when the ternary  $(\text{Fe}_{1-x}\text{Co}_x)_y\text{C}$  system is



(a)  $(\text{Fe}_{1-x}\text{Co}_x)_8\text{C}$     (b)  $(\text{Fe}_{1-x}\text{Co}_x)_{16}\text{C}$     (c)  $(\text{Fe}_{1-x}\text{Co}_x)_{24}\text{C}$     (d)  $(\text{Fe}_{1-x}\text{Co}_x)_{32}\text{C}$   
*Figure 4.1.* Illustrations of the various  $(\text{Fe}_{1-x}\text{Co}_x)_y\text{C}$  structures with interstitial C atoms studied in Papers I and II.

grown on a CuAu buffer the tetragonal strain saturates towards  $c/a \approx 1.03$  as the film is grown thicker, in contrast to the binary  $\text{Fe}_{1-x}\text{Co}_x$  system which rapidly saturates towards  $c/a = 1$ , clearly indicating that the C atoms indeed induce a tetragonal strain. A magnetocrystalline anisotropy as large as  $E_{\text{MAE}} = 0.44 \text{ MJ/m}^3$  was measured for  $x = 0.6$ . However, only a small C content of around 2 at.% appears to enter the system which makes direct comparison to data in Paper I difficult. Hence, calculations were performed for a  $(\text{Fe}_{0.4}\text{Co}_{0.6})_{32}\text{C}$  system as that illustrated in Fig. 4.1d with the experimentally measured lattice parameters  $a = 2.81$  and  $c/a = 1.03$ . Calculations using WIEN2k with VCA and force theorem indicate  $E_{\text{MAE}} = 0.51 \text{ MJ/m}^3$  while SPR-KKR with CPA and total energy differences yields  $E_{\text{MAE}} = 0.22 \text{ MJ/m}^3$ . The experimental value is in between the two theoretical ones and theory and experiment can be considered to be in good agreement. One would, however, expect the CPA to provide a more reliable result than the VCA but in this case the VCA result is slightly closer to the experimental value.

#### 4.1.2 $(\text{Fe}_{1-x}\text{Co}_x)\text{-B}$

If it is possible for C to go into interstitial positions, as discussed above, it is easy to imagine also other atoms with similar size and properties, such as B or N, to do the same. Consequently, the procedure performed in Paper I was repeated with B substituting C and the results, shown in Table 4.1, are overall similar. What can be noted is, however, that the tetragonal strain and thus also the MAE, is now larger for systems with  $y = 24$  than what was the case with C. Hence, it appears that compared to C impurities, low amounts of B can cause larger tetragonal strains and thus lead to higher MAE per impurity content.

**Table 4.1.**  $c/a$  and MAE of various  $(\text{Fe}_{1-x}\text{Co}_x)_y\text{B}$  systems.

Composition	$c/a$	$\text{MAE}_{\text{torque}} (\frac{\mu\text{eV}}{\text{atom}})$	$\text{MAE} (\frac{\mu\text{eV}}{\text{atom}})$	$\text{MAE} (\frac{\text{MJ}}{\text{m}^3})$
$(\text{Fe}_{0.5}\text{Co}_{0.5})_8\text{B}$	1.247	76.2	104.6	1.51
$(\text{Fe}_{0.35}\text{Co}_{0.65})_{16}\text{B}$	1.116	15.5	40.3	0.58
$(\text{Fe}_{0.4}\text{Co}_{0.6})_{16}\text{B}$	1.103	31.1	48.7	0.69
$(\text{Fe}_{0.45}\text{Co}_{0.55})_{16}\text{B}$	1.091	43.8	48.3	0.69
$(\text{Fe}_{0.50}\text{Co}_{0.50})_{16}\text{B}$	1.086	41.3	43.5	0.62
$(\text{Fe}_{0.35}\text{Co}_{0.65})_{24}\text{B}$	1.083	21.0	37.1	0.53
$(\text{Fe}_{0.4}\text{Co}_{0.6})_{24}\text{B}$	1.079	31.2	41.8	0.59
$(\text{Fe}_{0.45}\text{Co}_{0.55})_{24}\text{B}$	1.076	36.1	41.3	0.58
$(\text{Fe}_{0.50}\text{Co}_{0.50})_{24}\text{B}$	1.074	39.7	44.4	0.63

The results in Table 4.1 were calculated with SPR-KKR and the CPA and the MAE was evaluated both using the torque method and as difference of total energies. Although the MAE is of the same order of magnitude when calculated with the two methods, the agreement is far from excellent and for some cases, such as that of  $(\text{Fe}_{0.35}\text{Co}_{0.65})_{16}\text{B}$ , there is a discrepancy by more than a factor two. Similar problems occurred when studying the  $(\text{Fe}_{1-x}\text{Co}_x)\text{-C}$  systems in the previous section so it appears that the torque method, or at least the implementation utilised here, is not reliable for these systems. This is in contrast to the case of  $\text{Fe}_{1-x}\text{Co}_x$  as was seen in Fig. 3.2 which implies that the local distortion introduced by the C or B makes the torque method inappropriate.

## 4.2 $\text{L1}_0$ Binary Compounds

Fig. 4.2 illustrates two different unit cells of the  $\text{L1}_0$  crystal structure, one fct-like cell with volume  $V_1 = a^2c$  and one bct-like rotated by  $\frac{\pi}{4}$  with volume  $V_2 = a'^2c = \frac{V_1}{2}$ . The structure is often described in terms of the fct-like structure but for computations it is beneficial to use the smaller bct-like structure to reduce the system size and hence also computational effort. Certain binary alloys, such as FePt [82, 83, 84, 85], can exhibit enormous MAE in this ordered structure. Interestingly, it is sometimes possible to obtain large MAE also without heavy elements such as Pt, providing large SOC, and materials of this kind have received attention for permanent magnet applications. In Paper III a thorough investigation into the electronic structure and magnetic properties of the binary alloys FeNi [23, 82, 86, 87, 88, 24], CoNi [89], MnAl [90, 91, 92, 93] and MnGa [94, 95, 96] is presented. In addition to the evaluation of  $M_S$  and MAE via DFT,  $T_C$  is also calculated using MC simulations to obtain a complete picture of the three important permanent magnet properties. It is found that under certain circumstances all of the investigated

compounds exhibit interesting properties from a permanent magnet perspective.

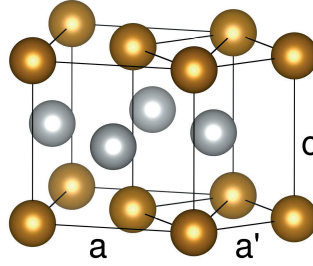


Figure 4.2. Illustration of two different perspectives on the  $L1_0$  structure.

MAE and  $M_S$  are significant in all of the compounds, although  $M_S$  is smaller in the Mn-based materials which also contain a non-magnetic element. In FeNi and CoNi, also the  $T_C$  is found to be high but by studying substitutional disorder, where there is intermixing of the atoms in the two different sublattices, it is found that both  $T_C$  and, in particular, MAE decrease notably, even for rather small amounts of disorder.

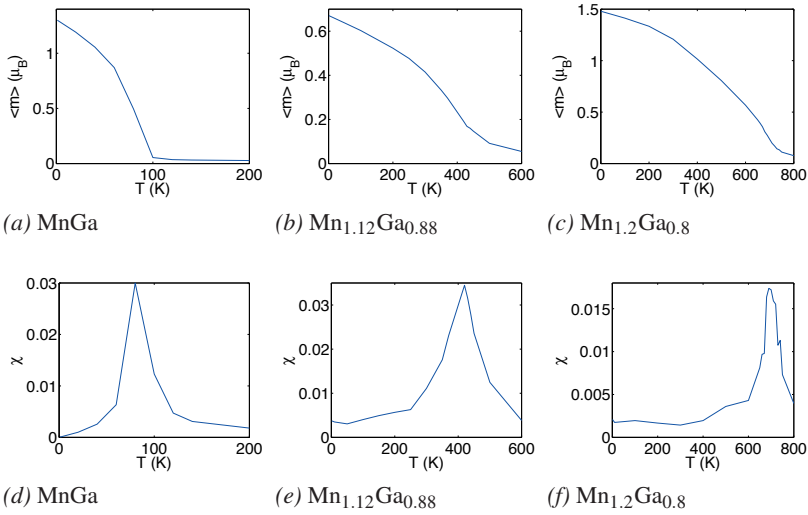


Figure 4.3. Average moments and susceptibility as functions of temperature for MnGa,  $Mn_{1.12}Ga_{0.88}$  and  $Mn_{1.2}Ga_{0.8}$ .

In the case of Mn-based materials, there often occur strongly antiferromagnetic exchange interactions for Mn atoms which are at a short distance from one another, which destabilises the ferromagnetic state. As a consequence, MnAl exhibits a antiferromagnetic ground state while MnGa is only very weakly ferromagnetic with  $T_C = 70$  K. It turns out, however, that a ferrimag-

netic state with significant Curie temperature up to  $T_C \approx 700$  K is attainable in both compounds by going off-stoichiometry and adding excess Mn into the second sublattice. Fig. 4.3 shows the effect of increasing the Mn-content in MnGa on the average moment and susceptibility as function of temperature, as found from MC simulations in UppASD. It is clear that the phase transition occurs for higher temperatures with higher Mn-content, which appears to be consistent with experimental observations [96]. Fig. 4.4 illustrates the resulting ferrimagnetic ordering.

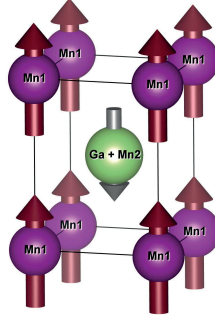


Figure 4.4. Ferrimagnetic  $\text{Mn}_{1+x}\text{Ga}_{1-x}$

## 4.3 Other Potential Materials

Various other materials have been discussed as potential candidates for replacement permanent magnets without rare earths or Pt. One candidate which has received interest is  $\text{Fe}_2\text{P}$ , due to its huge MAE [19], but unfortunately it has rather low  $T_C$  which might however be possible to raise by alloying with small amounts of other elements [97, 98, 99, 100, 101]. Another candidate which has shown potential as a permanent magnet is MnBi [102, 103, 104] with the anomalous behaviour of an MAE which increases strongly with temperature [105]. Two other materials which could posses interesting properties are  $(\text{Fe}_{1-x}\text{Co}_x)_2\text{B}$  and Heusler alloys which will be described further in the coming two Sections 4.3.1-4.3.2.

### 4.3.1 $(\text{Fe}_{1-x}\text{Co}_x)_2\text{B}$

The tetragonal  $(\text{Fe}_{1-x}\text{Co}_x)_2\text{B}$  system, in the space group 140 structure shown in Fig. 4.5, with four equivalent Fe/Co atoms and two equivalent B atoms, was studied by Iga [106] and for certain values of  $x$  it exhibits a relatively large uniaxial MAE. Consequently, by tuning the composition of Fe and Co it might be possible to obtain a material with the desired properties for a useful hard magnet.

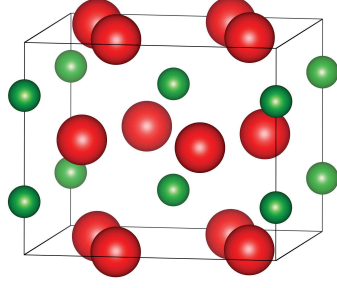


Figure 4.5. One unit cell of  $(\text{Fe}_{1-x}\text{Co}_x)_2\text{B}$ . Large, red balls represent Fe/Co atoms, while the small green balls represent B atoms.

Fig. 4.6 contains results of SPR-KKR calculations with alloying treated within the CPA and MAE evaluated by the torque method. Fig. 4.6a and Fig. 4.6b show the saturation magnetisation and MAE as functions of  $x$  and it is revealed that the MAE is uniaxial in the region  $0.1 \leq x \leq 0.6$  with a maximum value of  $E_{\text{MAE}} = 0.77 \text{ MJ/m}^3$  around  $x = 0.3$ . The saturation magnetisation is a monotonously decreasing function of  $x$  since Co has a smaller moment than that of Fe but even at the cobalt rich side it remains reasonably high around  $\mu_0 M_S = 1.0 \text{ T}$ .

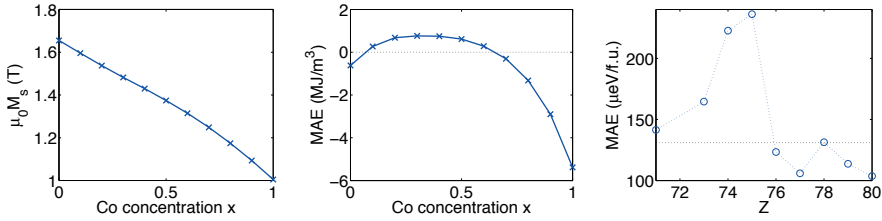


Figure 4.6. Magnetisation and MAE as functions of  $x$  in  $(\text{Fe}_{1-x}\text{Co}_x)_2\text{B}$  as well as MAE for various atomic numbers  $Z$  in  $(\text{Fe}_{0.675}\text{Co}_{0.275}\text{Z}_{0.05})_2\text{B}$ .

Hybridisation effects can induce increased MAE even by adding non-magnetic elements which contribute with strong SOC [107]. One possible route to further increasing the MAE of the material could therefore be to add heavier elements from a few rows down in the periodic table. Fig. 4.6c shows the effect on MAE of exchanging 5 at.% of Fe and Co for various elements of atomic number  $Z$  from the 5d row of elements (Hf is missing because a well converged calculation was not obtained) with a dotted line indicating the value obtained for the ternary system. It appears from these results that only the first elements in the row are useful for this purpose and W and Re seem particularly useful as they allow for a two-fold increase of the MAE.

### 4.3.2 Heusler Alloys

The Heusler alloys consist of a wide range of materials with tunable properties making them interesting for a variety of applications [108]. Most of the Heusler alloys are cubic but some can exist in a tetragonal phase [108, 109] allowing for the possibility of finding materials with large MAE. It appears that most magnetic tetragonal Heuslers are Mn-based of the form  $\text{Mn}_2\text{YZ}$  and can exhibit large MAE but tend to be ferrimagnetic with rather low magnetic moments. The case of  $\text{Y}=\text{Mn}$ ,  $\text{Z}=\text{Ga}$ , shown in Fig. 4.7, exhibits an enormous MAE as the results of FP-LAPW calculations in WIEN2k presented in Table 4.2 show.

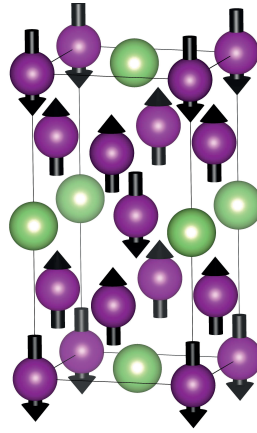


Figure 4.7. The  $\text{DO}_{22}$  tetragonal Heusler structure of  $\text{Mn}_3\text{Ga}$  with arrows indicating magnetic moments on the Mn atoms.

As seen in Fig. 4.8, the ferrimagnetic state with the magnetic ordering shown in Fig. 4.7 is favoured over a ferromagnetic state by around 0.4 eV. The ferrimagnetic ordering also appears to favour a slightly larger distance between atoms, with larger volume and  $c/a$  than would be the case for a ferromagnetic structure and it allows for an even larger value of the MAE than what would have been the case for ferromagnetic ordering.

With the large MAE of  $E_{\text{MAE}} = 1.3 \text{ MJ/m}^3$  observed in ferrimagnetic  $\text{Mn}_3\text{Ga}$  it could have significant potential as a permanent magnet. Unfortunately, the total moment in the unit cell is only  $m = 1.76\mu_{\text{B}}$ , corresponding to a saturation magnetisation of  $\mu_0 M_{\text{S}} = 0.20 \text{ T}$  making it less suitable. Similar systems could be of interest if elements which tend to prefer ferromagnetic alignment, such as Fe, could be used as a substitute for Mn. However, it appears that such materials tend to prefer the cubic phase [110] resulting in tiny MAE and making them less suitable in the context of interest.



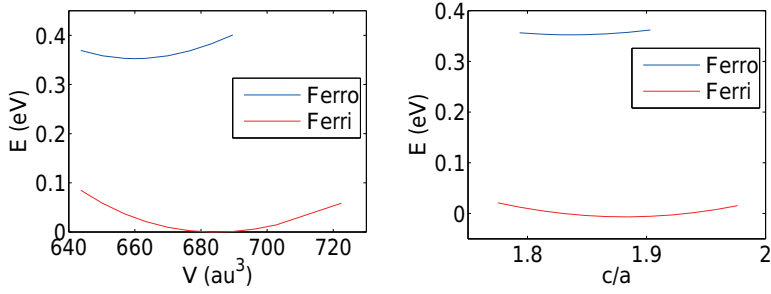


Figure 4.8. Total energy as a function of volume and  $c/a$  for ferro- or ferrimagnetic  $\text{Mn}_3\text{Ga}$ .

**Table 4.2.** Table summarising the properties of ferro- and ferrimagnetic  $\text{Mn}_3\text{Ga}$ .

Quantity	Ferro $\text{Mn}_3\text{Ga}$	Ferri $\text{Mn}_3\text{Ga}$
$a$ (a.u.)	7.11	7.13
$c$ (a.u.)	13.07	13.44
$a$ (Å)	3.76	3.77
$c$ (Å)	6.92	7.11
$m_{\text{Mn-1}}$ ( $\mu_B$ )	0.68	-2.79
$m_{\text{Mn-2}} = m_{\text{Mn-3}}$ ( $\mu_B$ )	2.17	2.28
$m_{\text{Ga}}$ ( $\mu_B$ )	-0.05	-0.03
$E_{\text{MAE}}$ ( $\mu\text{eV/f.u.}$ )	532.8	830.1

## 5. Conclusions

After giving a brief background to the theory of magnetism most relevant to understanding permanent magnets and an introduction to computational methods suitable to study permanent magnet material properties, a number of rare-earth free materials with promising properties for the given purpose have been presented. In particular, a novel material consisting of an FeCo alloy with C atoms causing a tetragonal distortion with a resulting increased MAE has been presented based on theoretical work and then also in an experimental realisation. In addition to this, the properties of various binary alloys in the  $L1_0$  structure have been thoroughly assessed and turn out to exhibit highly interesting properties if a high degree of ordering in the right alloy concentrations is achieved. An overview has also been given over other materials with potentially useful properties.

Obtaining good permanent magnets without the use of heavy elements such as rare-earths or Pt is indeed a challenging task but it is clear that solutions exist. More specifically it has been seen that with the correct band structure around the Fermi energy, a large MAE can be obtained with only 3d elements and this can be improved further through hybridisation effects via non-magnetic elements with stronger spin-orbit coupling. As illustrated in Fig. 5.1, a number of promising materials have already been found with properties which are at least superior to the ferrite magnets and the search continues for more alternatives. The last step on the path towards novel permanent magnets will then be for the experimental side of the research community to provide efficient methods of synthesis and characterisation.

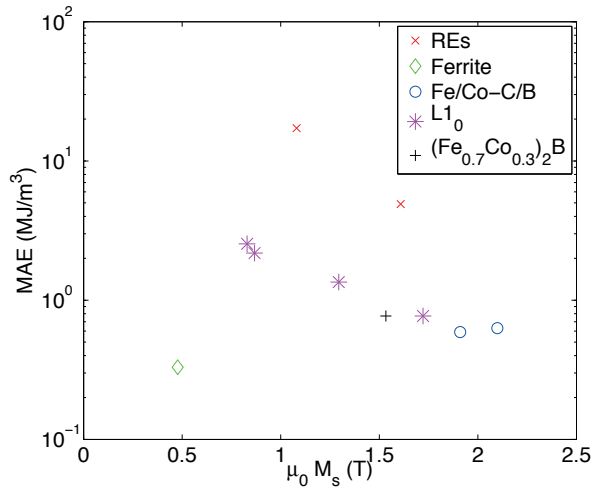


Figure 5.1. Summarising comparison of permanent magnet properties for materials presented in this thesis and existing rare-earth and ferrite alternatives.

# References

- [1] J. M. D. Coey, “Advances in Magnetism Hard Magnetic Materials : A Perspective,” *IEEE Transactions on Magnetism*, vol. 47, no. 12, pp. 4671–4681, 2011.
- [2] J. Coey, “Permanent magnets: Plugging the gap,” *Scripta Materialia*, vol. 67, pp. 524–529, Sept. 2012.
- [3] J. M. D. Coey, “Permanent Magnetism,” *Solid State Communications*, vol. 102, no. 2, pp. 101–105, 2000.
- [4] L. H. Lewis and F. Jiménez-Villacorta, “Perspectives on Permanent Magnetic Materials for Energy Conversion and Power Generation,” *Metallurgical and Materials Transactions A*, vol. 44, pp. 2–20, July 2012.
- [5] R. Skomski and J. M. D. Coey, *Permanent Magnetism*. Institute of Physics Publishing, 1999.
- [6] D. Kramer, “Concern grows over China’s dominance of rare-earth metals,” *Physics Today*, vol. 63, no. 5, p. 22, 2010.
- [7] R. Skomski, *Simple Models of Magnetism*. Oxford University Press, 2008.
- [8] S. Chikazumi, *Physics of Ferromagnetism*. Oxford University Press, 1997.
- [9] G. E. Uhlenbeck and S. Goudsmit, “Ersetzung der Hypothese vom ummechanischen Zwang durch eine Forderung Besüglic des inneren Verhaltens jedes einzelnen Elektrons,” *Die Naturwissenschaften*, vol. 13, pp. 953–954, 1925.
- [10] P. A. M. Dirac, “The Quantum Theory of the Electron.,” *Proceedings of the Royal Society A*, vol. 117, no. 778, pp. 610–624, 1928.
- [11] P. A. M. Dirac, “The Quantum Theory of the Electron. Part II,” *Proceedings of the Royal Society A: Mathematical, Physical and Engineering Sciences*, vol. 118, pp. 351–361, Mar. 1928.
- [12] F. Gross, *Relativistic Quantum Mechanics and Field Theory*. John Wiley & Sons, Inc., 1993.
- [13] T. Ohlsson, *Relativistic Quantum Physics*. Cambridge University Press, 2011.
- [14] J. H. V. Vleck, “On the Anisotropy of Cubic Ferromagnetic Crystals,” *Physical Review*, vol. 52, pp. 1178–1198, 1937.
- [15] N. W. Ashcroft and D. N. Mermin, *Solid State Physics*. Belmont, USA: Brooks/Cole, 1976.
- [16] P. Mohn, *Magnetism in the Solid State An Introduction*. Springer-Verlag, 2002.
- [17] H. Brooks, “Ferromagnetic Anisotropy and the Itinerant Electron Model,” *Physical Review*, vol. 58, 1940.
- [18] T. Burkert, L. Nordström, O. Eriksson, and O. Heinonen, “Giant Magnetic Anisotropy in Tetragonal FeCo Alloys,” *Physical Review Letters*, vol. 93, p. 027203, July 2004.
- [19] M. Costa, O. Grånäs, A. Bergman, P. Venezuela, P. Nordblad, M. Klintonberg, and O. Eriksson, “Large magnetic anisotropy of Fe<sub>2</sub>P investigated via ab initio

- density functional theory calculations,” *Physical Review B*, vol. 86, p. 085125, Aug. 2012.
- [20] R. Wu and A. Freeman, “Spin-orbit induced magnetic phenomena in bulk metals and their surfaces and interfaces,” *Journal of Magnetism and Magnetic Materials*, vol. 200, pp. 498–514, Oct. 1999.
- [21] P. Bruno, “Tight-binding approach to the orbital magnetic moment and magnetocrystalline anisotropy of transition-metal monolayers,” *Physical Review B*, vol. 39, no. 1, pp. 865–868, 1989.
- [22] C. Andersson, B. Sanyal, O. Eriksson, L. Nordström, O. Karis, D. Arvanitis, T. Konishi, E. Holub-Krappe, and J. Dunn, “Influence of Ligand States on the Relationship between Orbital Moment and Magnetocrystalline Anisotropy,” *Physical Review Letters*, vol. 99, p. 177207, Oct. 2007.
- [23] Y. Miura, S. Ozaki, Y. Kuwahara, M. Tsujikawa, K. Abe, and M. Shirai, “The origin of perpendicular magneto-crystalline anisotropy in  $L1_0$ -FeNi under tetragonal distortion,” *Journal of physics. Condensed matter : an Institute of Physics journal*, vol. 25, p. 106005, Mar. 2013.
- [24] M. Kotsugi, M. Mizuguchi, S. Sekiya, M. Mizumaki, T. Kojima, T. Nakamura, H. Osawa, K. Kodama, T. Ohtsuki, T. Ohkochi, K. Takanashi, and Y. Watanabe, “Origin of strong magnetic anisotropy in  $L1_0$ -FeNi probed by angular-dependent magnetic circular dichroism,” *Journal of Magnetism and Magnetic Materials*, vol. 326, pp. 235–239, Jan. 2013.
- [25] W. Nolting and A. Ramakanth, *Quantum Theory of Magnetism*. Springer-Verlag, 2009.
- [26] J. Ruzs, L. Bergqvist, J. Kudrnovský, and I. Turek, “Exchange interactions and Curie temperatures in  $Ni_{2-x}MnSb$  alloys: First-principles study,” *Physical Review B*, vol. 73, p. 214412, Jun 2006.
- [27] Pajda, M. and Kudrnovský, J. and Turek, I. and Drchal, V. and Bruno, P., “Ab initio calculations of exchange interactions, spin-wave stiffness constants, and Curie temperatures of Fe, Co, and Ni,” *Physical Review B*, vol. 64, p. 174402, Oct 2001.
- [28] D. Bonnenberg, K. A. Hempel, and H. P. J. Wijn, *Figs. 94 - 114, Tables 18 - 19*, vol. 19a of *Landolt-Börnstein - Group III Condensed Matter*, ch. 3d, 4d and 5d Elements, Alloys and Compounds. Springer, 1986.
- [29] H. Eschrig, *The Fundamentals of Density Functional Theory*. Dresden, 2003.
- [30] J. M. Wills, M. Alouani, P. Andersson, A. Delin, O. Eriksson, and O. Grechnev, *Full-Potential Electronic Structure Method*. Springer, 2010.
- [31] R. M. Martin, *Electronic Structure*. Cambridge University Press, 2004.
- [32] D. P. Landau and K. Binder, *A Guide to Monte Carlo Simulations in Statistical Physics*. Cambridge University Press, 2000.
- [33] P. Hohenberg and W. Kohn, “Inhomogeneous Electron Gas,” *Physical Review*, vol. 136, no. 1962, pp. 864–871, 1964.
- [34] W. Kohn and L. J. Sham, “Self-Consistent Equations Including Exchange and Correlation Effects,” *Physical Review*, vol. 140, no. 4a, pp. 1133–1138, 1965.
- [35] L. O. Wagner, T. E. Baker, E. M. Stoudenmire, K. Burke, and S. R. White, “Kohn-sham calculations with the exact functional,” *Physical Review B*, vol. 90, p. 045109, Jul 2014.
- [36] A. Zunger and J. P. Perdew, “Self-interaction correction to density-functional

- approximations for many-electron systems,” *Physical Review B*, vol. 23, no. 10, pp. 5048–5079, 1981.
- [37] J. P. Perdew and Y. Wang, “Accurate and simple analytic representation of the electron-gas correlation energy,” *Physical Review B*, vol. 45, pp. 13244–13249, Jun 1992.
  - [38] J. P. Perdew, K. Burke, and M. Ernzerhof, “Generalized Gradient Approximation Made Simple,” *Physical Review Letters*, vol. 77, pp. 3865–3868, Oct. 1996.
  - [39] G. Kotliar, S. Savrasov, K. Haule, V. Oudovenko, O. Parcollet, and C. Marianetti, “Electronic structure calculations with dynamical mean-field theory,” *Reviews of Modern Physics*, vol. 78, pp. 865–951, Aug. 2006.
  - [40] F. Tran, R. Laskowski, P. Blaha, and K. Schwarz, “Performance on molecules, surfaces, and solids of the Wu-Cohen GGA exchange-correlation energy functional,” *Physical Review B*, vol. 75, p. 115131, Mar 2007.
  - [41] V. Ozoliņš and M. Körling, “Full-potential calculations using the generalized gradient approximation: Structural properties of transition metals,” *Physical Review B*, vol. 48, pp. 18304–18307, Dec 1993.
  - [42] P. Bagno, O. Jepsen, and O. Gunnarsson, “Ground-state properties of third-row elements with nonlocal density functionals,” *Physical Review B*, vol. 40, pp. 1997–2000, Jul 1989.
  - [43] S. Cottenier, *Density Functional Theory and the Family of (L)APW-methods: a step-by-step introduction*. Instituut voor Kern- en Stralingsfysica, K.U.Leuven, Belgium, 2002.
  - [44] P. Blaha, G. Madsen, K. Schwarz, D. Kvasnicka, and J. Luitz, “WIEN2k, An Augmented Plane Wave + Local Orbitals Program for Calculating Crystal Properties,” 2001.
  - [45] O. K. Andersen, “Linear methods in band theory,” *Physical Review B*, vol. 12, pp. 3060–3083, Oct 1975.
  - [46] J. C. Slater, “Wave functions in a periodic potential,” *Physical Review*, vol. 51, pp. 846–851, May 1937.
  - [47] D. D. Koelling and H. N. Harmon, “A technique for relativistic spin-polarised calculations,” *Journal of Physics C: Solid State Physics*, vol. 10, 1977.
  - [48] A. H. MacDonald, W. E. Pickett, and D. D. Koelling, “A linearised relativistic augmented-plane-wave method utilising approximate pure spin basis functions,” *Journal of Physics C: Solid State Physics*, vol. 13, pp. 2675–83, 1980.
  - [49] H. Ebert, “The Munich SPR-KKR package, version 6.3,” 2012.
  - [50] H. Ebert, D. Ködderitzsch, and J. Minár, “Calculating condensed matter properties using the KKR-Green’s function method -recent developments and applications,” *Reports on Progress in Physics*, vol. 74, p. 096501, Sept. 2011.
  - [51] J. Korringa, “On the calculation of the energy of a bloch wave in a metal,” *Physica*, vol. 13, no. 6-7, pp. 392 – 400, 1947.
  - [52] E. N. Economou, *Green’s Functions in Quantum Physics*. Springer Berlin Heidelberg, 2006.
  - [53] J. Zabludil, R. Hammerling, P. Weinberger, and L. Szunyogh, *Electron Scattering in Solid Matter*. Springer, 2005.
  - [54] J. S. Faulkner and G. M. Stocks, “Calculating properties with the

- coherent-potential approximation,” *Physical Review B*, vol. 21, pp. 3222–3244, Apr 1980.
- [55] J. S. Faulkner, “The modern theory of alloys,” *Progress in Materials Science*, vol. 27, no. 1–2, pp. 1–187, 1982.
  - [56] A. Zunger, S.-H. Wei, L. G. Ferreira, and J. E. Bernard, “Special quasirandom structures,” *Physical Review Letters*, vol. 65, pp. 353–356, Jul 1990.
  - [57] P. James, *Calculation of magnetism and its crystal structure dependence*. PhD thesis, Uppsala University, 1999.
  - [58] P. Söderlind, B. Johansson, and O. Eriksson, “Spin and orbital magnetism in Fe-Co and Co-Ni alloys,” *Journal of Magnetism and Magnetic Materials*, vol. 45, June 1992.
  - [59] I. Turek, J. Kudrnovský, and K. Carva, “Magnetic anisotropy energy of disordered tetragonal Fe-Co systems from ab initio alloy theory,” *Physical Review B*, vol. 86, p. 174430, Nov. 2012.
  - [60] C. Neise, S. Schönecker, M. Richter, K. Koepernik, and H. Eschrig, “The effect of chemical disorder on the magnetic anisotropy of strained Fe-Co films,” *Physica Status Solidi (B)*, vol. 248, pp. 2398–2403, Oct. 2011.
  - [61] P. Soven, “Coherent-Potential Model of Substitutional Disordered Alloys,” *Physical Review*, vol. 156, no. 3, 1967.
  - [62] P. E. Blöchl, O. Jepsen, and O. K. Andersen, “Improved tetrahedron method for Brillouin-zone integrations,” *Physical Review B*, vol. 49, no. 23, 1994.
  - [63] A. I. Liechtenstein, M. I. Katsnelson, V. P. Antropov, and V. A. Gubanov, “Local Spin Density Functional Approach To The Theory Of Exchange Interactions In Ferromagnetic Metals And Alloys,” *Journal of Magnetism and Magnetic Materials*, vol. 67, pp. 65–74, 1987.
  - [64] G. H. O. Daalderop, P. J. Kelly, and M. F. H. Schuurmans, “First-principles calculation of the magnetocrystalline anisotropy energy of iron, cobalt, and nickel,” *Physical Review B*, vol. 41, pp. 11919–11937, Jun 1990.
  - [65] X. Wang, R. Wu, D. Wang, and A. Freeman, “Torque method for the theoretical determination of magnetocrystalline anisotropy,” *Physical Review B*, vol. 54, pp. 61–64, July 1996.
  - [66] J. Staunton, L. Szunyogh, a. Buruzs, B. Györffy, S. Ostanin, and L. Udvardi, “Temperature dependence of magnetic anisotropy: An ab initio approach,” *Physical Review B*, vol. 74, p. 144411, Oct. 2006.
  - [67] A. I. Liechtenstein, M. I. Katsnelson, and V. A. Gubanov, “Exchange interactions and spin-wave stiffness in ferromagnetic metals,” *Journal of Physics F: Metal Physics*, vol. 14, 1984.
  - [68] A. I. Liechtenstein, M. I. Katsnelson, V. P. Antropov, and V. A. Gubanov, “LSDF-Approach to the theory of exchange interactions in magnetic metals,” *Journal of Magnetism and Magnetic Materials*, vol. 54–57, pp. 965–966, 1986.
  - [69] B. Skubic, J. Hellsvik, L. Nordström, and O. Eriksson, “A method for atomistic spin dynamics simulations: implementation and examples,” *Journal of Physics: Condensed Matter*, vol. 20, p. 315203, Aug. 2008.
  - [70] R. K. Pathria, *Statistical Mechanics*. Elsevier, 2nd ed., 1996.
  - [71] M. Wallin, *Monte Carlo Simulations in Statistical Physics*. KTH, Stockholm, Sweden, 2005.
  - [72] N. Metropolis, A. W. Rosenbluth, M. N. Rosenbluth, A. H. Teller, and

- E. Teller, "Equation of state calculations by fast computing machines," *The Journal of Chemical Physics*, vol. 21, no. 6, pp. 1087–1092, 1953.
- [73] A. R. Williams, V. L. Moruzzi, A. P. Malozemoff, and K. Terakura, "Generalized Slater-Pauling Curve for Transition-Metal Magnets," *IEEE Transactions on Magnetics*, vol. 19, no. 5, pp. 1983–1988, 1983.
- [74] G. Andersson, T. Burkert, P. Warnicke, M. Björck, B. Sanyal, C. Chacon, C. Zlotea, L. Nordström, P. Nordblad, and O. Eriksson, "Perpendicular Magnetocrystalline Anisotropy in Tetragonally Distorted Fe-Co Alloys," *Physical Review Letters*, vol. 96, p. 037205, Jan. 2006.
- [75] F. Yildiz, M. Przybylski, X.-D. Ma, and J. Kirschner, "Strong perpendicular anisotropy in  $\text{Fe}_{1-x}\text{Co}_x$  alloy films epitaxially grown on mismatching Pd(001), Ir(001), and Rh(001) substrates," *Physical Review B*, vol. 80, p. 064415, Aug. 2009.
- [76] P. Warnicke, G. Andersson, M. Björck, J. Ferré, and P. Nordblad, "Magnetic anisotropy of tetragonal FeCo/Pt(001) superlattices," *Journal of Physics: Condensed Matter*, vol. 19, p. 226218, June 2007.
- [77] D. Bonnenberg, K. A. Hempel, and H. P. J. Wijn, *1.2.1 Alloys between Fe, Co or Ni, 1.2.1.1 Phase diagrams, lattice parameters*, vol. 19a of *Landolt-Börnstein - Group III Condensed Matter*, ch. 3d, 4d and 5d Elements, Alloys and Compounds. Springer, 1986.
- [78] G. Kurdjumov, "Martensite crystal lattice, mechanism of austenite-martensite transformation and behavior of carbon atoms in martensite," *Metallurgical Transactions A*, vol. 7, no. 7, pp. 999–1011, 1976.
- [79] R. Naraghi, M. Selleby, and J. A. gren, "Thermodynamics of stable and metastable structures in Fe-C system," *Calphad*, vol. 46, no. 0, pp. 148 – 158, 2014.
- [80] G. Kurdjumov and A. Khachaturyan, "Nature of axial ratio anomalies of the martensite lattice and mechanism of diffusionless  $\gamma \rightarrow \alpha$  transformation," *Acta Metallurgica*, vol. 23, no. 9, pp. 1077 – 1088, 1975.
- [81] L. C. Materials Science International Team MSIT, Andy Watson, *Carbon - Cobalt - Iron, iron systems: phase diagrams, crystallographic and thermodynamic data, 1.2.1.1 Phase diagrams, lattice parameters*, vol. 11D1: Iron Systems, Part 1 of *Landolt-Börnstein - Group IV Physical Chemistry*, ch. 3d, 4d and 5d Elements, Alloys and Compounds. Springer, 2008.
- [82] Y. Kota and A. Sakuma, "Relationship between Magnetocrystalline Anisotropy and Orbital Magnetic Moment in  $\text{L1}_0$  -Type Ordered and Disordered Alloys," *Journal of the Physical Society of Japan*, vol. 81, pp. 1–6, 2012.
- [83] T. Burkert, O. Eriksson, S. Simak, A. Ruban, B. Sanyal, L. Nordström, and J. Wills, "Magnetic anisotropy of  $\text{L1}_0$  FePt and  $\text{Fe}_{1-x}\text{Mn}_x\text{Pt}$ ," *Physical Review B*, vol. 71, p. 134411, Apr. 2005.
- [84] J. B. Staunton, S. Ostanin, S. S. A. Razee, B. Gyroffy, L. Szunyogh, B. Ginatempo, and E. Bruno, "Long-range chemical order effects upon the magnetic anisotropy of FePt alloys from an ab initio electronic structure theory," *Journal of Physics: Condensed Matter*, vol. 16, pp. S5623–S5631, Dec. 2004.
- [85] P. Ravindran, a. Kjekshus, H. Fjellvåg, P. James, L. Nordström, B. Johansson, and O. Eriksson, "Large magnetocrystalline anisotropy in bilayer transition



- metal phases from first-principles full-potential calculations,” *Physical Review B*, vol. 63, p. 144409, Mar. 2001.
- [86] T. Kojima, M. Mizuguchi, and K. Takanashi, “L1<sub>0</sub>-ordered FeNi film grown on Cu-Ni binary buffer layer,” in *Journal of Physics: Conference Series*, vol. 266, p. 012119, Jan. 2011.
- [87] L. Néel, J. Pauleve, R. Pauthenet, J. Laugier, and D. Dautreppe, “Magnetic Properties of an Iron-Nickel Single Crystal Ordered by Neutron Bombardment,” *Journal of Applied Physics*, vol. 35, no. 3, p. 873, 1964.
- [88] T. Kojima, M. Mizuguchi, T. Koganezawa, K. Osaka, M. Kotsugi, and K. Takanashi, “Magnetic Anisotropy and Chemical Order of Artificially Synthesized L1<sub>0</sub>-Ordered FeNi Films on Au-Cu-Ni Buffer Layers,” *Japanese Journal of Applied Physics*, vol. 51, p. 010204, Jan. 2012.
- [89] S. Fukami, H. Sato, M. Yamanouchi, S. Ikeda, and H. Ohno, “CoNi Films with Perpendicular Magnetic Anisotropy Prepared by Alternate Monoatomic Layer Deposition,” *Applied Physics Express*, vol. 6, p. 073010, July 2013.
- [90] A. J. J. Koch, P. Hokkelling, M. G. v. d. Steeg, and K. J. de Vos, “New Material for Permanent Magnets on a Base of Mn and Al,” *Journal of Applied Physics*, vol. 31, no. 5, p. S75, 1960.
- [91] J. H. Park, Y. K. Hong, S. Bae, J. J. Lee, J. Jalli, G. S. Abo, N. Neveu, S. G. Kim, C. J. Choi, and J. G. Lee, “Saturation magnetization and crystalline anisotropy calculations for MnAl permanent magnet,” *Journal of Applied Physics*, vol. 107, no. 9, p. 09A731, 2010.
- [92] S. H. Nie, L. J. Zhu, J. Lu, D. Pan, H. L. Wang, X. Z. Yu, J. X. Xiao, and J. H. Zhao, “Perpendicularly magnetized  $\tau$ -MnAl (001) thin films epitaxied on GaAs,” *Applied Physics Letters*, vol. 102, no. 15, p. 152405, 2013.
- [93] J. M. D. Coey, “New permanent magnets; manganese compounds,” *Journal of physics. Condensed matter : an Institute of Physics journal*, vol. 26, p. 064211, Jan. 2014.
- [94] A. Sakuma, “Electronic structures and magnetism of CuAu-type MnNi and MnGa,” *Journal of Magnetism and Magnetic Materials*, vol. 187, pp. 105–112, Aug. 1998.
- [95] K. Wang, E. Lu, J. W. Knepper, F. Yang, and A. R. Smith, “Structural controlled magnetic anisotropy in Heusler L1<sub>0</sub>-MnGa epitaxial thin films,” *Applied Physics Letters*, vol. 98, no. 16, p. 162507, 2011.
- [96] E. Lu, D. Ingram, A. Smith, J. Knepper, and F. Yang, “Reconstruction Control of Magnetic Properties during Epitaxial Growth of Ferromagnetic Mn<sub>3</sub>Ga on Wurtzite GaN(0001),” *Physical Review Letters*, vol. 97, p. 146101, Oct. 2006.
- [97] R. Fruchart, “Crystallographic and Magnetic Properties of Solid Solutions of the Phosphides M<sub>2</sub>P, M = Cr, Mn, Fe, Co, and Ni,” *Journal of Applied Physics*, vol. 40, no. 3, p. 1250, 1969.
- [98] Catalano, A. and Arnott, R. J. and Wold, A, “Magnetic and Crystallographic Properties of the System Fe<sub>2</sub>P<sub>1-x</sub>As<sub>x</sub>,” *Journal of Solid State Chemistry*, vol. 7, pp. 262–268, 1973.
- [99] C. Jian-wang, L. He-lie, and Z. Qing-qi, “Electronic structures and magnetic properties of Fe<sub>2</sub>P and the effects of doping with Ni,” *Journal of Physics: Condensed Matter*, vol. 5, pp. 9307–9316, 1993.
- [100] S. N. Doli, A. Krishnamurthy, V. Ghose, and B. K. Srivastava, “Magnetic

- behaviour of Ni-substituted  $\text{Fe}_2\text{P}$ ,” *Journal of Physics: Condensed Matter*, vol. 5, pp. 451–458, 1993.
- [101] J. Leitão, M. van der Haar, a. Lefering, and E. Brück, “Magnetic and magnetocaloric exploration of Fe rich  $(\text{Mn,Fe})_2(\text{P,Ge})$ ,” *Journal of Magnetism and Magnetic Materials*, vol. 344, pp. 49–54, Oct. 2013.
- [102] A. Sakuma, Y. Manabe, and Y. Kota, “First Principles Calculation of Magnetocrystalline Anisotropy Energy of  $\text{MnBi}$  and  $\text{MnBi}_{1-x}\text{Sn}_x$ ,” *Journal of the Physical Society of Japan*, vol. 82, no. 7, p. 73704, 2013.
- [103] N. V. R. Rao, A. M. Gabay, W. F. Li, and G. C. Hadjipanayis, “Nanostructured bulk  $\text{MnBi}$  magnets fabricated by hot compaction of cryomilled powders,” *Journal of Physics D: Applied Physics*, vol. 46, no. 26, p. 265001, 2013.
- [104] N. V. R. Rao, A. M. Gabay, and G. C. Hadjipanayis, “Anisotropic fully dense  $\text{MnBi}$  permanent magnet with high energy product and high coercivity at elevated temperatures,” *Journal of Physics D: Applied Physics*, vol. 46, no. 6, p. 062001, 2013.
- [105] P. A. Albert and W. J. Carr, “Temperature Dependence of Magnetostriction and Anisotropy in  $\text{MnBi}$ ,” *Journal of Applied Physics*, vol. 32, no. 3, pp. S201–S202, 1961.
- [106] A. Iga, “Magnetocrystalline Anisotropy in  $(\text{Fe}_{1-x}\text{Co}_x)_2\text{B}$  System,” *Japanese Journal of Applied Physics*, vol. 9, pp. 415–416, 1970.
- [107] S. Bhandary, O. Grånäs, L. Szunyogh, B. Sanyal, L. Nordström, and O. Eriksson, “Route towards finding large magnetic anisotropy in nanocomposites: Application to a  $\text{W}_{1-x}\text{Re}_4/\text{Fe}$  multilayer,” *Physical Review B*, vol. 84, p. 092401, Sept. 2011.
- [108] T. Graf, C. Felser, and S. S. Parkin, “Simple rules for the understanding of Heusler compounds,” *Progress in Solid State Chemistry*, vol. 39, pp. 1–50, May 2011.
- [109] C. Felser, V. Alijani, J. Winterlik, S. Chadov, and A. K. Nayak, “Tetragonal Heusler Compounds for Spintronics,” *IEEE Transactions on Magnetics*, vol. 49, no. 2, pp. 682–685, 2013.
- [110] J. Kiss, S. Chadov, G. H. Fecher, and C. Felser, “Disorder-induced cubic phase in  $\text{Fe}_2$ -based Heusler alloys,” *Physical Review B*, vol. 87, p. 224403, June 2013.